

**Synthesis and characterization of V
and Gd substituted Cobalt Ferrite
nanoparticles**



Afeera Zara Naz

Student ID: anaz.msphy19sns

Reg. No: 00000321179

Session 2019-2021


Supervised by

Dr. Faheem Amin

**DEPARTMENT OF PHYSICS
SCHOOL OF NATURAL SCIENCES (SNS)
NATIONAL UNIVERSITY OF SCIENCE AND TECHNOLOGY
H12, ISLAMABAD, PAKISTAN
OCTOBER 2021**

National University of Sciences & Technology**MS THESIS WORK**

We hereby recommend that the dissertation prepared under our supervision by: Afeera Zara Naz, Regn No. 00000321179 Titled: "Synthesis and Characterization of V and Gd Substituted Cobalt Ferrite Nanoparticles" accepted in partial fulfillment of the requirements for the award of **MS** degree.

Examination Committee Members1. Name: PROF. SYED RIZWAN HUSSAINSignature: 2. Name: DR. FAHAD AZADSignature: External Examiner: DR. WAQAS KHALIDSignature: Supervisor's Name: DR. FAHEEM AMINSignature: 


Head of Department

15.02.2022
Date

COUNTERSIGNEDDate: 15.02.2022


Dean/Principal

Declaration

I certify that this research work titled “Synthesis and characterization of Vanadium and Gadolinium substituted cobalt ferrite nanoparticles” is my own work. The work has not been presented elsewhere for assessment. The material that has been used from other sources has been properly acknowledged/referred.

Signature of Student:

Afeera Zara Naz

2019-NUST-MS-PHY-00000321179

Copyright Statement

Copyright in text of this thesis rests with the student author. Copies (by any process) either in full, or of extracts, may be made only in accordance with instructions given by the author and lodged in the Library of NUST School of Natural Sciences (SNS). Details may be obtained by the Librarian. This page must form part of any such copies made. Further copies (by any process) may not be made without the permission (in writing) of the author.

The ownership of any intellectual property rights which may be described in this thesis is vested in NUST School of Natural Sciences, subject to any prior agreement to the contrary, and may not be made available for use by third parties without the written permission of the SNS, which will prescribe the terms and conditions of any such agreement.

Further information on the conditions under which disclosures and exploitation may take place is available from the Library of NUST School of Natural Sciences, Islamabad.

Acknowledgment

I am thankful to Allah, my Creator, for guiding me through this endeavor at every step and for every new notion He implanted in my head to help me improve my work. Without Your invaluable assistance and direction, I would have been unable to do anything. It was Your will that whoever supported me over the duration of my thesis, whether it was my parents or anybody else, therefore no one else is worthy of praise but You.

I would also like to thank my supervisor, Dr. Faheem Amin, for his unwavering support and advice during my thesis, as well as for providing me with resources for my research. I would like to express my gratitude to him for assisting me in learning and for giving me his precious time and attention. I am also thankful all my faculty members especially my GEC members "Dr. Rizwan Hussain and Dr. Fahad" of school of natural sciences (SNS) for their polite and kind behavior. They guide me well whenever I went to them in any problem. I not even learned my subjects from them effectively but also to be a helping and honest as a person in my life.

I would also like to thank my siblings, Sibtain, Abdul Saboor, Burrera, and Paryab for their unwavering faith in me. Thank you to Ms. Ghousia, Ms. Samia and Mr. Ejaz for always being a major inspiration and encouragement to me.

I am grateful to my friends Aroosa, Anum, Kainat, Iqra, Dr. Sidra, Annu, Shabnum, Summera, Wafa, Yousiara, Dr. Neha and Khola for accompanying me during my master's degree.

This is dedicated to my lovely grandparents, Muhammad Amin and Nighat saba, as well as my parents, Muhammad Zulfiqar and Naheed Akhtar whose unwavering support, selfless love, cooperation, and many prayers enabled me to achieve this wonderful accomplishment.

Contents

Table of Figures	11
List of tables	12
List of Abbreviations.....	13
Abstract	14
Chapter 1: Introduction	15
1.1: Categorisation of Nanomaterials.....	16
1.1.1: Zero-dimensional nanomaterial	16
1.1.2: One dimensional nanomaterial.....	16
1.1.3: Two-dimensional nanomaterial.....	16
1.1.4: Three-dimensional nanomaterials	16
1.2: Properties of Nanomaterials.....	17
1.2.1: Physical properties	17
1.2.2: Chemical properties	17
1.2.3: Electrical properties	17
1.2.4: Optical Properties.....	17
1.2.5: Magnetic Properties	18
1.3: Types of magnetic material.....	18
1.3.1: Paramagnetic Materials.....	18
1.3.2: Diamagnetic Materials	18
1.3.3: Ferromagnetism and Ferrimagnetism	19
1.3.4: Super-Para Magnetism.....	19
1.3.5: Anti-Ferromagnetism.....	19
1.4: Ferrites	20
1.4.1: Spinel ferrite.....	20
1.5: Types of Spinel Ferrites:	21

1.6: Ferritic Family	23
1.7: Significance of Ferrites	24
1.8: Application of Ferrites	25
Chapter 2: Literature Review	26
Chapter 3: Sample Preparation and Experimental Techniques.....	30
3.1: Methods of preparation	30
3.1.1: Solid state reaction method	30
3.1.2: Chemical method	30
3.2: Nanoparticle synthesis methods.....	30
3.2.1: Co-Precipitation	30
3.2.2: Sol-gel method	31
3.2.3: Hydrothermal method	31
3.2.4: Chemical Vapor Deposition.....	31
3.2.5: Sono-chemical Method	31
3.3: Chemical reagents used in Synthesis	32
3.4: Schematic diagram of samples preparation:	33
3.5: Characterization Techniques:.....	33
3.5.1: X-ray Diffraction.....	33
3.5.2 Scanning electron microscope.....	35
3.5.3: Energy dispersive X-ray Spectroscopy (EDS).....	36
3.5.4: Vibrating sample magnetometer	37
3.5.5: Brunauer-Emmet-Teller Theory (BET)	38
3.5.6: Particle size distribution (PSD).....	40
3.5.7: Fourier transform infrared spectroscopy (FTIR)	41
3.5.8: Raman spectroscopy	42
Chapter 4: Results and Discussion.....	45

4.1: Structural Analysis.....	45
4.2: Williamson Hall Analysis	48
4.3: Morphological and compositional Analysis	50
4.4: Magnetic measurements.....	53
4.5: BET Analysis	54
4.6: Particle size distribution Measurements	56
4.6: FTIR spectroscopy	57
4.7: Raman Spectroscopy.....	59
Chapter 5: Conclusion.....	62
References	63

Table of Figures

Figure 1: Illustration of Nanoscale objects	15
Figure 2: Categories of nanomaterials [1]	16
Figure 3: Paramagnetic atomic dipole configuration	18
Figure 4: Diamagnetic atomic dipole configuration	19
Figure 5: Anti-Ferromagnetic atomic dipole configuration	20
Figure 6: a) Spinel unit cell structure, (b) octahedral, c) tetrahedral interstice	21
Figure 7: Schematic diagram of samples preparation	33
Figure 8: Characterisation Techniques	33
Figure 9: Description of X-ray Diffraction instruments	34
Figure 10: Principle of X-ray diffraction and illustrating Bragg's Law.	34
Figure 11: Schematic illustration of SEM instrument	36
Figure 12: Vibrating sample magnetometer principle and working.....	37
Figure 13 B-H hysteresis loop obtained from VSM	38
Figure 14: Schematic representation of BET surface area measurement instrument.....	40
Figure 15: Laser Diffraction Particle size analysis principle	40
Figure 16: Block diagram of Michelson Interferometer Apparatus	42
Figure 17: Schematic diagram of Raman Apparatus	44
Figure 18: X-ray diffraction patterns obtained for (a) $\text{CoFe}_{2-x}\text{V}_x\text{O}_4$ (b) $\text{CoFe}_{2-x}\text{Gd}_x\text{O}_4$	46
Figure 19: Variation of Crystallite size of (a) CVFO (b) CGFO, lattice parameter of (c) CVFO (d) CGFO, and X-ray density (e) CVFO (f) CGFO.....	48
Figure 20: W-H plot of (a) CFO 500 (b) CFO 900 (c) V 2% (d) V 5% (e) V 10% (f) Gd 2% (g) Gd 5% (h) Gd 10%.....	49
Figure 21: SEM micrographs and the corresponding EDS spectrum of (a,b) for CFO 500 (c,d) for CFO 900 .	50
Figure 22: Room-temperature M-H loops for prepared nano samples	54
Figure 23: BET adsorption isotherm of (a) CFO 500 (b) CFO 900 (c) V 2% (d) V 5% (e) V 10% (f) Gd 2% (g) Gd 5% (h) Gd 10%	56
Figure 24: Infra-red absorption spectra of CFO500, CFO900, V and Gd doped CFO prepared samples	59

List of tables

Table 1: Different types of Ferrites	23
Table 2: Comparison of soft and hard Ferrites	24
Table 3: Reagents, Formula, Molecular mass, and Radii of some common metal ions used in the synthesis of spinel ferrites	32
Table 4: XRD : peak positions, FWHM (β), interplanar distance (d), crystallite size (D), lattice parameter (a), Volume (V), Density (ρ) of prepared nanoparticles	47
Table 5: Magnetic properties of samples, coercivity (H_c), saturation magnetization (M_s), remanent magnetization (M_r), magneto crystalline anisotropy (K), molecular mass (M), Magnetic moment(μ)	54
Table 6: BET analysis of surface area, Langmuir surface area, BJH pore volume, BJH pore size, average particle size.....	56
Table 7: Particle size distribution of V and Gd doped cobalt ferrite nanoparticles.....	57
Table 8: Analysis of vibrational spectra FTIR of CFO500, CFO900, V and Gd doped CFO prepared samples.....	58

List of Abbreviations

RT	Room temperature
Fe	Iron
Co	Cobalt
O	Oxygen
V	Vanadium
Gd	Gadolinium
XRD	X-ray Diffraction
SEM	Scanning Electron Microscopy
BET	Brunauer Emmett Teller
FTIR	Fourier Transform Infrared
VSM	Vibrating sample magnetometer
EDS	Energy Dispersive X-ray Spectroscopy
FCO500	CoFe ₂ O ₄ annealed at 500°C
FCO900	CoFe ₂ O ₄ annealed at 900°C
CVFO	CoV _x Fe _{2-x} O ₄
2% V	CoV _x Fe _{2-x} O ₄ with 2% V (CoV _{0.02} Fe _{1.98} O ₄)
5% V	CoV _x Fe _{2-x} O ₄ with 5% V (CoV _{0.05} Fe _{1.95} O ₄)
10% V	CoV _x Fe _{2-x} O ₄ with 10% V (CoV _{0.1} Fe _{1.9} O ₄)
CGFO	CoGd _x Fe _{2-x} O ₄
2% Gd	CoGd _x Fe _{2-x} O ₄ with 2% Gd (CoGd _{0.02} Fe _{1.98} O ₄)
5% Gd	CoGd _x Fe _{2-x} O ₄ with 5% Gd (CoGd _{0.05} Fe _{1.95} O ₄)
10% Gd	CoGd _x Fe _{2-x} O ₄ with 10% Gd (CoGd _{0.1} Fe _{1.9} O ₄)

Abstract

In this work Vanadium and Gadolinium doped nanocrystalline cobalt ferrite $\text{CoM}_x\text{Fe}_{2-x}\text{O}_4$, where M represents V or Gd and $x= 0\%$, 2% , 5% and 10% were synthesized by coprecipitation method. The undoped sample was annealed at 500 and 900°C . It was found that the crystallite size increased with increasing annealing temperature. The doped samples were therefore annealed at 900°C . The formation of a cubic spinel phase was confirmed by XRD. The crystallite sizes of the V doped samples were calculated to be between 39 and 44nm , while the crystallite sizes of the Gd doped samples ranged from 35 to 47nm . According to XRD, the crystallite size improved with sintering temperature. With V doping, particle size showed a decreasing trend, followed by an increasing trend. This is because V replaced iron in the octahedral location, reducing crystallite size, but as doping concentration increased more than 5% , Fe began to move towards the tetrahedral site, increasing crystallite size. The crystallite size was found to lower because of Gd substitution. SEM imaging was used to study the morphology of ferrites. In SEM images, nanocrystalline particles can be seen arranged into layers with a porous structure. The presence of Co, Fe, V and Gd elements in the samples was shown by EDX analysis. According to FTIR measurements, the vibrational peaks associated with octahedral and tetrahedral sites vary with doping. PSD analysis showed the formation of particle agglomeration. BET adsorption isotherm was used to calculate the specific area of samples. Using VSM, magnetic properties such as coercivity, retentivity, and saturation magnetization were determined. According to the VSM study, all samples were ferromagnetic. Doping increased remanence magnetization.

Chapter 1: Introduction

The term nano is a prefix that refers to a billionth of a metre (10^{-9}m), which is around the length of a few hydrogen atoms or nearly a hundredth thousand times the thickness of human hair. Changes in physical attributes are expected occur when microparticles become nanoparticles due to increased surface to volume ratio. This aspect contributes to the rising dominance of atoms on the surface of a particle in isolation and their interaction with other materials. Figure 1 depicts a variety of man-made and natural objects with nanometre-scale dimensions. Nanofibers, and core-shell nanofibers offer a high potential for polymer-based composites with diverse applications such as sensors, catalysts, environmental applications, filter applications, industrial applications, optoelectronics, and so on.

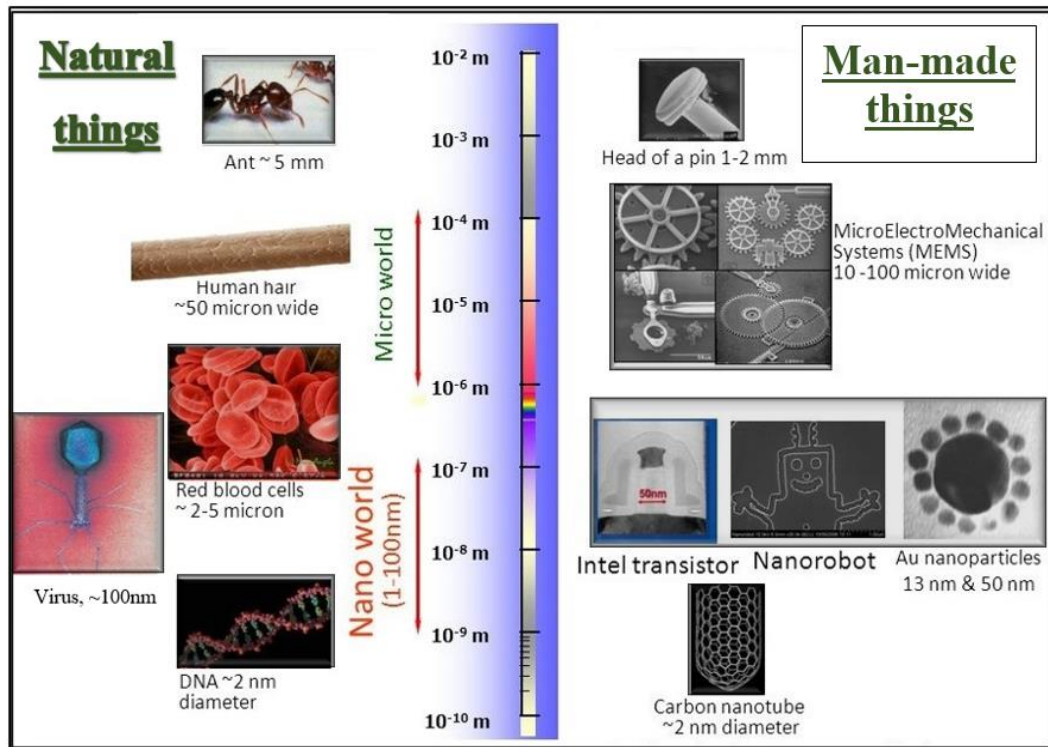


Figure 1: Illustration of Nanoscale objects

1.1: Categorisation of Nanomaterials

Nanomaterials are classified into four types based on their dimensions

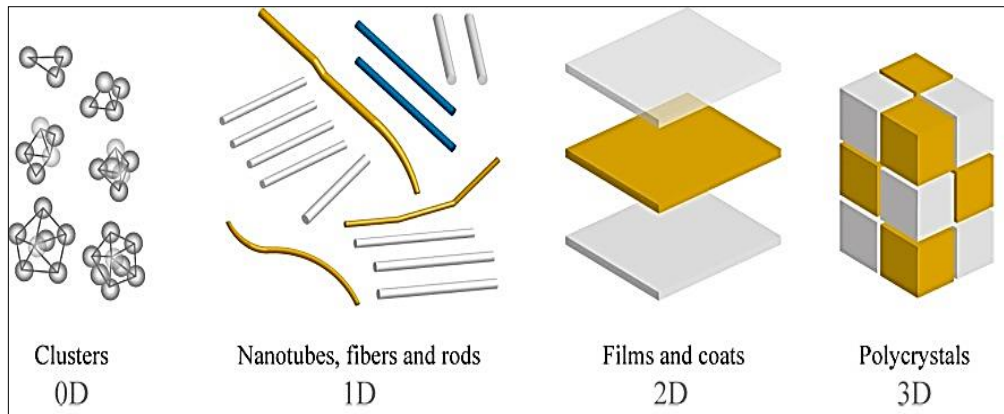


Figure 2: Categories of nanomaterials [1]

1.1.1: Zero-dimensional nanomaterial

All three of the zero-dimensional nanomaterials are restricted to the nanoscale range. Nanoparticles, nano-shells, and quantum dots are examples of zero-dimensional materials.

1.1.2: One dimensional nanomaterial

One-dimensional materials are those which one dimension is limited to the nanoscale. Electrons in these materials can move freely in one dimension. Nanotubes, nanowires, nanorods, and nanofibers are examples of one-dimensional nanomaterials.

1.1.3: Two-dimensional nanomaterial

Materials in which two dimensions are restricted to the nanoscale (100nm). Electrons in these materials are constrained in one dimension but have free movement in the other two. Nanofilms, nanolayers, and nanocoating are examples of two-dimensional nanomaterials.

1.1.4: Three-dimensional nanomaterials

Bulk materials are another name for three-dimensional nanomaterials. These materials, despite not being limited to the nanoscale range (100nm), have unique and fascinating properties due to the presence of nanostructures. It is made up of nanowire, nanotube, and other nanostructure clusters.

1.2: Properties of Nanomaterials

1.2.1: Physical properties

The physical properties of macroscopic materials measured in the laboratory under normal conditions include boiling points, melting points, conductivities, and so on.

Structure, which includes defect structure and crystallinity.

Size distribution

Surface topography/morphology

Agglomeration/aggregation state

Solubility

1.2.2: Chemical properties

Structural formula or molecular structure

Nanomaterial composition and degree of purity

Surface chemistry

1.2.3: Electrical properties

The electrical properties of nanoparticles are related to electrical conductivity or, conversely, electrical resistivity. Because of their small dimensions, nanomaterials have enhanced effects on electrical properties. It has been discovered that decreasing particle size causes an increase in electrical resistance because the size of the nanoparticle is very small and the number of electron wave modes participating in conduction decreases in quantized steps. Metallic nanomaterial conductivity decreases as particle size decreases, and these particles behave as non-conducting, below critical size, and temperature.

1.2.4: Optical Properties

The optical band gap expands when particle size decreases, notably in semiconductor nanomaterials. Spherical gold nanomaterials with a diameter of 25 nm, for example, appear green, whereas those with a diameter of 100 nm seem orange.[1]

1.2.5: Magnetic Properties

Magnetization levels measured at 10kOe were observed to decrease with decreasing NP size. Nanoparticles less than 3nm in size were discovered to become paramagnetic, indicating that inert surface layer takes precedence. As a result, the magnetic characteristics of the ferrite nanoparticles alter. [2]

1.3: Types of magnetic material

1.3.1: Paramagnetic Materials

Paramagnetic materials weakly magnetize in direction of magnetizing field permanent magnetic dipole because of partial cancelation of orbital magnetic moment and orbital spin. When applied magnetization is removed there is no net macroscopic magnetization. [4]

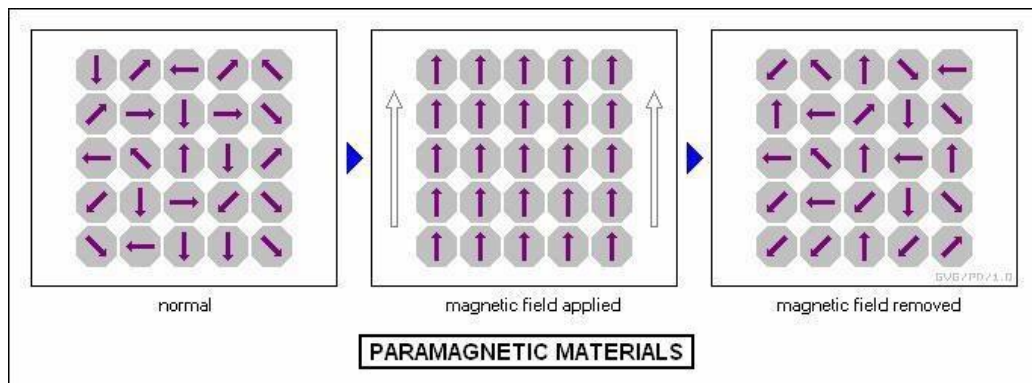


Figure 3: Paramagnetic atomic dipole configuration

1.3.2: Diamagnetic Materials

When placed in a magnetic field, these materials become weakly magnetised in the opposite direction of the applied field. When a magnetic field is applied, electrons travel in orbitals around an atom, causing diamagnetism. Orbital motion is responsible for the formation of a magnetic field that is diametrically opposed to the applied magnetic field. As a result, in the case of magnetic materials, an atom net magnetic moment is zero. Magnetization in these materials returns to zero as soon as the magnetic field is withdrawn because thermal intrinsic energy is greater than potential energy, which aligns the dipole, and dipole moments tend to randomise due to thermal agitation.[5]

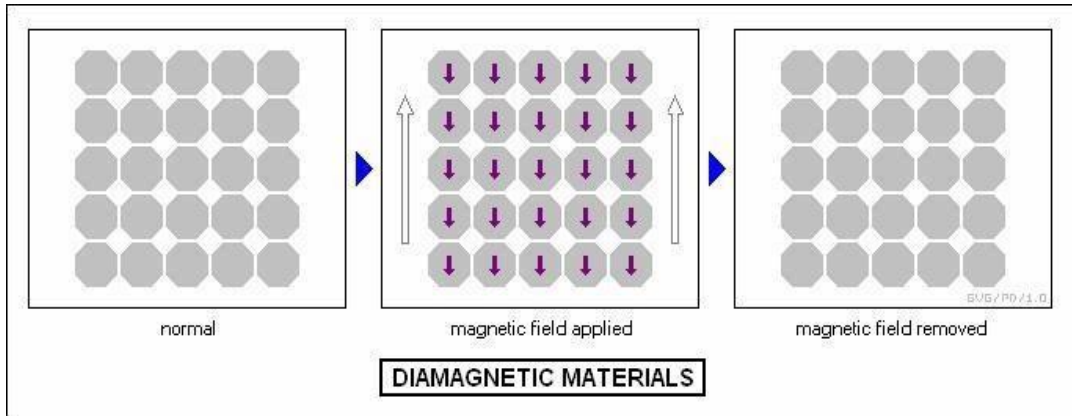
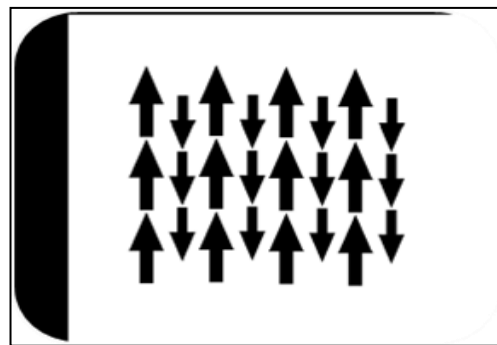
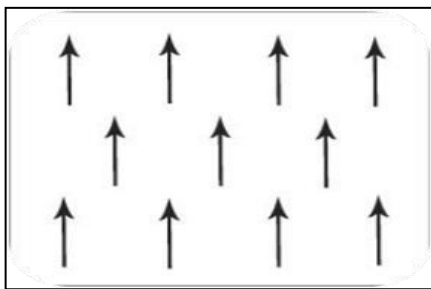


Figure 4: Diamagnetic atomic dipole configuration

1.3.3: Ferromagnetism and Ferrimagnetism

Ferromagnetic and ferrimagnetic materials are those that have persistent magnetization even after the removal of an external magnetic field. These have high permanent magnetization values. Atomic spins, also known as domains, interact with one another in such a way that all spins align in the same direction. The permanent magnetization exhibited in ferromagnetic materials is caused by insufficient magnetic field cancellation. This will result in permanent magnetism of a low magnitude. If all the dipoles in the sample align, their aggregate results in macroscopic magnetization in ferromagnetic and ferrimagnetic materials. Ionic solids and ferromagnetic materials are both electrically insulating. Metals are the most common ferromagnetic materials. [6]



1.3.4: Super-Para Magnetism

When a material is treated at temperatures lower than the Curie temperature, super-para-magnetism occurs. This aligns the magnetic moments of nearby atoms. [7]

1.3.5: Anti-Ferromagnetism

Anti-ferromagnetism is caused by magnetic moments or electron spins aligned in a regular pattern to the spins of surrounding atoms but oriented in the opposite

direction. This type of activity is exhibited at very low temperatures and disappears above a certain temperature. This is referred to as “Neel temperature.” [7]

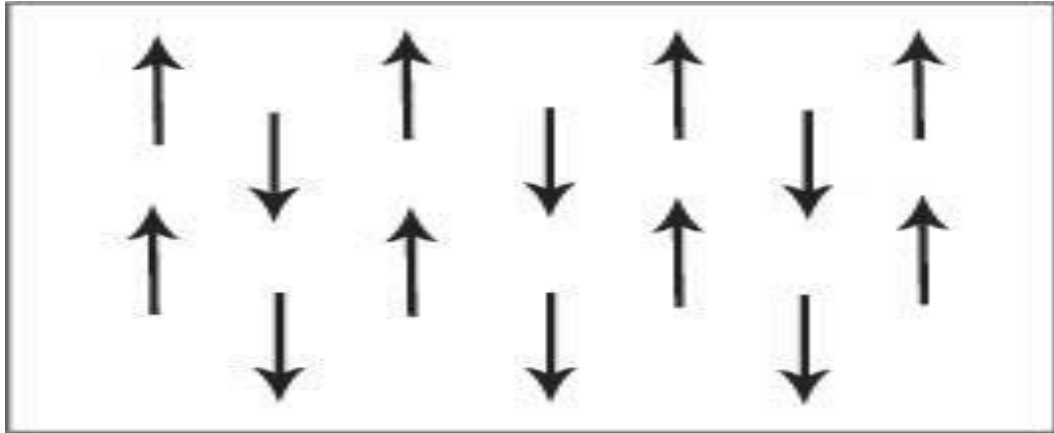


Figure 5: Anti-Ferromagnetic atomic dipole configuration

1.4: Ferrites

The most important ferrimagnetic materials are ferrites. The main component of ferrites is iron oxide (Fe_2O_3). Due to the presence of ferrimagnetic oxides, ferrites are insulating materials. Ferrites are a magnetic family of materials that are used to manufacture cores for transformers, permanent magnets, and a variety of other uses. They are primarily used in high frequency applications where they limit the production of eddy currents because of their high resistivity. [9]

Metal oxide and iron oxide are major elements of ferrites. Ferrites are classified into following groups depending on their crystal structure.

1.4.1: Spinel ferrite

Spinel ferrites are also known as cubic ferrites. The formula AB_2O_4 describes the crystalline phase of spinel ferrite, where A denotes metal ion like Zn^{+2} , Mg^{+2} , Cd^{2+} , Ni^{2+} , Co^{2+} , Fe^{2+} or a mixture of these ions like $\text{Co}_{0.5} \text{Zn}_{0.5}$ or $\text{Co}_{0.5} \text{Zn}_{0.5}$ and B is a trivalent cation such as iron or aluminium. These spinel ferrites have a cubical unit cell structure, (Figure 4) with each unit cell made up of eight smaller unit cells called “octanes” or “formula units”. The chemical formula is $\text{M}_8\text{Fe}_{16}\text{O}_{32}$. Each unit cell is made up of 32 oxygen atoms in a face-centred cubic lattice containing tetrahedral and octahedral sites. Six oxygen atoms surround the octahedral sites, which are referred known as B sites. When metal ions of 2+ or 3+ valency are introduced into the A and B sites. Due to existence of a positive charge, the spinel ferrite structure is not electrically neutral. [8]

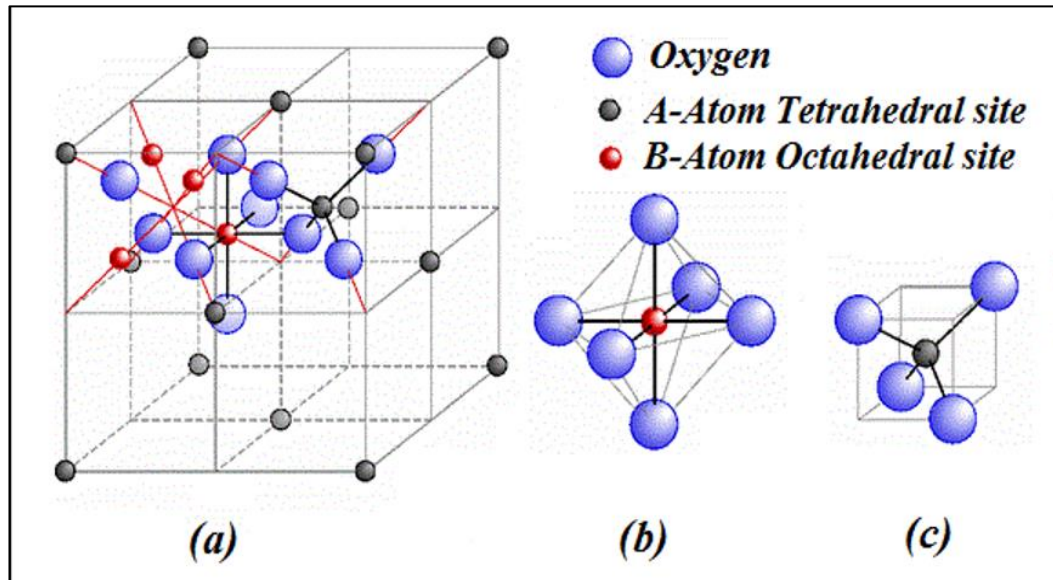


Figure 6: a) Spinel unit cell structure, (b) octahedral, (c) tetrahedral interstice

Tetrahedral sites

The interstitial is inserted in the centre of the tetrahedral (A) generated by four lattice atoms at the tetrahedral (A) site. Three atoms are on the plane in a symmetrical formation, while the fourth atom is on top. Only 8 of the system's 64 tetrahedral (A) sites are occupied for charge neutrality. Each unit cell in an FCC has eight tetrahedral (A) sites. Figure 4 (b)

Octahedral sites

The interstitial is in the core of an octahedral (B) form by 6 lattice atoms in an octahedral (B) site. Four atoms are in a plane, touching each other; the other two atoms are in a symmetrical position on top and bottom of the plane. In a spinel structure, 16 octahedral (B) sites out of 32 are occupied for charge neutrality. An octahedral position in an FCC lattice is depicted in the figure 4(c).

1.5: Types of Spinel Ferrites:

“Two types of spinel structure are there:

Normal spinel

Inverse spinel

In normal ferrites, all trivalent metal ions are present at the B sites, and all the divalent metal ions occupy the A sites in the crystal structure.

In inverse spinel ferrites, trivalent ions occupy both the A and B sites, and all divalent metal ions occupy the B sites in the crystal structure. [9]

Garnet Ferrites

The second group of ferrites is garnets, which have the general formula $A_3B_5O_{12}$, where A is a rare earth metal cation such as yttrium, and B is iron. Garnet ferrites have a cubical unit cell with eight smaller formula units. Garnet ferrites have tetrahedral A sites, octahedral B sites, and dodecahedral C sites. The iron cations (Fe^{3+}) are distributed in the A and B sites in a 3:2 ratio, while the dodecahedral C sites are occupied by Me cations surrounded by oxygen atoms. Garnet is well-known for its optical transparency and magneto-optical properties. [8]

Ortho Ferrites

Orthoferrites are a third type of ferrite with a distorted perovskite structure and a general formula of ABX_3 , where A is a rare earth or alkaline metal cation, B is a transition metal cation, usually iron, and X is an anionic element, usually oxygen. The central ion, Fe, forms an octahedron in orthoferrites, which is coordinated by six oxygen atoms. The A cations, which are coordinated by 12 oxygen atoms, fill the interstitial spaces in the octahedral structure. Ortho ferrites have high domain wall velocities and are used in magnetic field sensors, communication techniques, and electrical current, among other things. [8]

Hexagonal Ferrites:

The general formula for hexagonal ferrites is $MFe_{12}O_{19}$. M can be cobalt, strontium, barium, or a mixture of these elements. Because of their strong coercivity, hexagonal ferrites are used as permanent magnets [9]. The hexagonal structure resembles the spinel structure. Metal ions occupy three distinct locations in the structure. These are octahedral, tetrahedral, and trigonal sites. These magnetic materials are widely employed in a variety of fields, including magnetic recording devices, refrigerator magnets, microwave applications, and loudspeakers. The table below provides a summary of several crystal structured ferrites and their examples

Type	Structure	General Formula	Example
Spinel	Cubic	$M^{II}Fe_2O_4$	$M^{II}=Fe, Cd, Co, Mg, Ni$ and Zn
Garnet	Cubic	$M^{III}_3Fe_2O_{12}$	$M^{III}=Y, Sm, Eu, Gd, Tb,$ and Lu
Magnetoplumbite	Hexagonal	$M^{II}Fe_{12}O_{19}$	$M^{II}=Ba, Sr$

Table 1: Different types of Ferrites

1.6: Ferritic Family

Ferrites based on the hysteresis losses and on their resistance to demagnetization, ferrites are classified into two categories

Hard ferrite

Demagnetization of hard ferrites is challenging due to their strong coercivity. Hard ferrite magnets provide reasonable electrical isolation and are difficult to demagnetize even in strong external magnetic fields. High coercivity indicates that the material takes a long time to demagnetize. The hard ferrites have a very high magnetic permeability. Among the most important hard ferrites are ferrite, strontium ferrite, and cobalt ferrite [9, 10].

Soft Ferrites

Soft ferrites are members of the ferritic family with very low coercivity. They are referred to as non-permanent magnets because they retain magnetism but lose it when the magnetic field is withdrawn. These are used to prevent energy losses in transformer and inductor cores. They frequently have performance criteria such as permeability and inductance. Soft ferrites include cobalt ferrite, nickel ferrite, and magnesium ferrite. [9] [10]

Soft ferrite	Hard ferrite
Low Saturated Magnetization	High saturated magnetization
Weak Coercivity (Hc)	Strong Coercivity (Hc)
Low Permeability	High Permeability
Weak Remanence	Strong Remanence
Low Magnetostriction	Strong Magnetostriction
Small Curie temperature (Tc)	Huge Curie temperature (Tc)

Table 2: Comparison of soft and hard Ferrites

1.7: Significance of Ferrites

Magnetic materials like iron and its alloys are used in various technologies. The reason for their use is their low DC resistivity. But some applications, like electrical circuits and cores of inductors, cannot make use of iron and its alloys as they require high frequencies. The current that is induced in the circuit starts flowing in the material. This results in heat generation due to the presence of low electrical resistivity. This will result in the release of energy into the atmosphere, posing serious issues. The energy losses make the material incompatible at high frequencies. The ferrites, on the other hand, showed better performance because of their high DC resistivity values. Their relatively high permeability and stability at high temperatures have also opened the way for their use in applications involving high frequencies like electronic circuits, adjustable inductors, filter circuits, and delay lines etc. Another reason for their use is that they are relatively less expensive as compared to other alloys. In case of material requirements that have low volume, high quality, low cost, and high stability, ferrites are best for frequency ranges of 10KHz to few MHz. Ferrites also offer flexible mechanical and magnetic parameters that none of the other metals offer [11].

Ferrites are commonly utilised because of the following properties [12]:

Easy production

Mechanical stiffness

Microwave applications

High frequency application

Diverse range of materials

High coercivity in selective ferrites

Considerable temperature and time stability

1.8: Application of Ferrites

Other applications of ferrites are given as under:

Pulse and wide band transformers

High density optical recording.

Power transformers and chokes.

Inductors and tuned transformers.

Rotating transformers

Magnetic shielding

Transducers.

Catalysis.

Drug delivery.

Optical properties.

Chapter 2: Literature Review

Spinel ferrites have piqued the curiosity of researchers because of their interesting physics and possible uses across a wide frequency range. These ferrites have a face-centred cubic structure with two interpenetrating sublattices, tetrahedral A-sites and octahedral B-sites. The substitution of other ions in A and B-sites, as well as their corresponding ratio, has a significant impact on the materials properties. The property enables researchers to combine many properties in a single ferrite and adapt them for specific purposes. Nanocrystalline spinel ferrites are a class of minerals with a wide range of uses, including high density storage media, microwave absorption materials, hypothermia for cancer treatment and magnetic drug delivery.

El-Shobaky et al synthesised cobalt ferrite nanoparticles after thermal treatment at 400-500°C and varying pH values. The impacts of calcination temperature and pH on the physicochemical, surface, and catalytic properties of generated ferrites were examined. As the calcination temperature increased, the crystalline size and degree of crystallinity increased, while the SBET values declined. The size of cobalt ferrite crystalline grew with increasing pH and coprecipitation temperature. [13]

Amiri et al. prepared Cobalt ferrites using a variety of processes, both traditional and chemical. Prepared nanoparticles were suitable for hyperthermia because of its high coercivity, strong (L-S) coupling, low superparamagnetic size at room temperature, high magnetic anisotropy energy, and mild saturation magnetization. It employed in magnetic separation due to high electrostatic interaction and suitable for MR imaging due to high relaxivity, anisotropy energy, and initial susceptibility. It can collaborate with drug delivery vehicles, which is especially important for chemotherapy. [14]

Coprecipitation approach was used to synthesize Co-Ni spinel ferrites. The Curie temperature became higher as the Ni content increased. The crystalline size was calculated using XRD. As a function of frequency, the dielectric constants and loss factors were also presented. [15]

Gul et al. produced a cubic spinel crystal from Zn-substituted CoFe_2O_4 . Because Zn has a larger radius than Co, the cell parameter increased linearly with Zn concentration while decreasing with curie temperature. The electrical resistance grew in parallel with the temperature. Ferrites' dielectric constant decreased with increasing frequency due to space charge polarization induced by electron displacement, which largely contributes to the dielectric constant. [16]

Goyal et al. used sol-gel technique to make magnetically separable $\text{CoMn}_{0.2}\text{Fe}_{1.8}\text{O}_4$ ferrite. The inexpensive cost of raw materials, ease of synthesis, recyclability, catalytic stability, and magnetic recoverability all drew attention to these nanoparticles. The synthetic nanomaterial has been developed as an environmentally safe and cost-effective nanocomposite and it is extremely convincing to handle industrial rudiments and environmental concerns soon. [17]

A hydrothermal approach was used to create nickel-doped cobalt ferrites. The sample's optical and magnetic characteristics were studied. Cation distribution investigations revealed that Ni^{+2} ions replaced Co^{+2} ions in octahedral B-sites. The presence of nickel influences magnetic properties. Ni-doped cobalt ferrite NPs are used in magnetic spintronics, actuators, and radar absorption materials. [18]

Zagaynov et al. synthesised Mn-Cu-Zr doped cobalt ferrite nanocomposites using co-precipitation technique and annealed samples at 1150 degrees Celsius. The sintered samples were fluorite-type ceria-based solid solutions with a single-phase cubic structure and a dense microstructure. In terms of material cost, these elements were more inexpensive than rare earth elements. [19]

Nohair et al. used thermogravimetry to evaluate the thermal behaviour of $\text{Fe}_{3-x}\text{V}_x\text{O}_4$, spinel's ($0 < x < 1$) produced by the ceramic method across the temperature range of 150-650°C. Kinetic investigations of V^{3+} ion oxidation at the B sites showed that the oxidation reaction was controlled by cation diffusion in a cation-deficient spinel phase of chemical composition. [20]

Heiba, et al. synthesised $\text{CoFe}_{2-x}\text{V}_x\text{O}_4$ (x ranges from 0 to 0.25), as well as $\text{CoFe}_{2-1.67x}\text{V}_x\text{O}_4$ (x is 0.1 and 0.2), using the sol gel method. According to both Rietveld and magnetic measurement investigations, vanadium occupied the B-site when x was less than 0.1 and transferred to the A site when x was greater than 0.1. The spin in A and B sites in CoFe_2O_4 was canted according to the Yafet-Kittel triangle

arrangement model, but the canted spin for $x > 0.0$ in $\text{CoFe}_{2-x}\text{V}_x\text{O}_4$ and $\text{CoFe}_{2-1.67x}\text{V}_x\text{O}_4$ systems was limited to B sites. [21]

Imanipour, et al. studied the effect of incorporating vanadium into magnetic material produced by sol-gel auto-combustion. Because vanadium atoms could not be totally replaced by cobalt atoms, two additional phases in vanadium-containing materials have been identified. According to FTIR analysis, all samples produced a cubic spinel phase. Secondary phases, average crystalline size variations, and magneto-crystallographic anisotropy were all associated with increased coercivity. [22]

Hossain et al. used solid-state reaction method to study manifests the outcomes of varying vanadium (V) concentration in Mn-Zn ferrites with the general composition $\text{Mn}_{0.6}\text{Zn}_{0.4}\text{V}_x\text{Fe}_{2-x}\text{O}_4$ ($x=0.00-0.10$, in steps of 0.02). X-ray diffraction (XRD) analysis of all the samples confirmed the formation of the spinel structure. The cell parameter slightly decreased with the increase in V content. The substitution of V noticeably enhanced densification in samples sintered at 1250°C . The grain size of the starting compositions varied from 13.0 to 27.9nm. The Fourier Transform Infrared (FTIR) spectra indicated the preference of vanadium ions at octahedral sites. The saturation magnetization (M_s) and the experimental magnetic moments ($1B$) are observed to increase for $x = 0.02$ with $M_s=61.73$ emu/g. This happened for the reduction of the A–B interaction in the AB_2O_4 spinel type ferrites. After that, M_s and μ ($1B$) values decreased for higher V contents. The magnetization obtained is explained by redistribution of cations in the tetrahedral and octahedral sites and spin canting due to weakening of exchange interaction. The complex modulus graphs were also studied to understand the mechanism of the electrical processes. [23]

Sodaee et al. synthesised Gadolinium substituted cobalt ferrite nanocrystals with composition of $\text{CoFe}_{2-x}\text{Gd}_x\text{O}_4$ ($x = 0-0.04$ in a step of 0.01) were prepared by a hydrothermal process and without subsequent annealing. X-ray diffraction, field-emission scanning electron microscopy, and vibrating sample magnetometer were used to investigate the effect of Gd^{3+} cation substitution on structural Characteristics and magnetic properties of cobalt ferrite nanocrystals. The X-ray diffraction analysis demonstrated that single phase spinel ferrites were obtained. The FE-SEM micrographs of the synthesized samples indicated the presence of two

distinct groups of grains exhibiting different sizes and, more important, different shapes. The results of magnetic hysteresis at a room temperature showed that with an increase in gadolinium content, the coercive field decreased from 1250Oe for $x = 0$ to 450Oe for $x = 0.03$. In addition, it was observed that with substitutions of gadolinium cations, the values of saturation magnetization decreased. [24]

Mugutkar et al. used Sol gel self-ignition method to successfully produce nanocrystalline gadolinium-substituted Co-Zn (CZG) ferrites. X-ray results confirmed the production of mono-phase spinel ferrites. According to Debye Scherer's formula, ferrite particle size decreases with Gd^{3+} substitution. According to the findings, substituting larger radii Gd^{3+} ions for smaller Fe^{3+} ions resulted in higher lattice parameter values. Changes in lattice parameters cause changes in bond length, tetra and octa edges, and hopping length differences. The increase in lattice parameter values was obtained by substituting smaller radius Gd^{3+} ions. Due to the magnitude of the qualities, the ferrites could be used in magnetic recording and storage systems. [25]

Chapter 3: Sample Preparation and Experimental Techniques

3.1: Methods of preparation

Ferrites can be prepared by two methods

1. Solid state reaction
2. Chemical method

3.1.1: Solid state reaction method

Dry technique is another name for solid state reaction process. Solid precursors are widely used in the synthesis of ferrites in powdered form. This approach has some limitations, including inhomogeneity and poor composition control. Chemical approaches have solved these advantages, resulting in ferrite nanoparticles that are homogenous, fine, and reproducible.

3.1.2: Chemical method

Chemical approach is also known as the wet chemical method. Chemistry has been instrumental in the development of novel materials with technologically significant qualities. Chemical processing has the advantage of chemical uniformity since it allows for molecule mixing. The reaction kinetics govern the production of ferrite nanoparticles. Controlling chemical homogeneity and stoichiometry necessitates meticulous reaction condition monitoring. In recent years, there has been a lot of effort on developing ferrites nanoparticles using unorthodox approaches, particularly chemical ones.

3.2: Nanoparticle synthesis methods

There are various methods for preparing nanoparticles, each having advantages and disadvantages. Different synthesis methods have different magnetic, structural, and electrical properties. The various synthesis approaches are as follows:

3.2.1: Co-Precipitation

In this method various chemicals that are normally soluble in aqueous or nonaqueous solutions are utilised. It involves the precipitation of salts aqueous

solution by addition of base (NaOH). The crystalline size can be adequately regulated by adjusting the reaction temperature and applying surface modification. The use of a mild oxidant in the reaction of metal salts with a base in aqueous environments results in the formation of nanoparticles. The pH of the solution, cation content, and presence of counter ions are all factors that determine the size and the phase of sample particles.

3.2.2: Sol-gel method

The sol-gel process is based on the colloidal chemistry. The method relies on the condensation and hydroxylation of molecular precursors in solution. To obtain the appropriate metal oxide framework, the sol obtained from non-metric ingredients is gelled or dried, either by eliminating the solvent or by executing a chemical reaction. The solvent in this method is usually water, but a base or an acid can be used to hydrolyse the precursors. The reaction is carried out at ambient temperature; however, heat treatment is required to acquire the final crystalline form.

3.2.3: Hydrothermal method

The hydrothermal process is used to create nanostructures at high temperature and pressure in a suitably closed system, such as an autoclave. Water is used as solvent in this method, so this is eco-friendly method. The sample obtained is filtered, centrifuged, and annealed at proper temperature.

3.2.4: Chemical Vapor Deposition

In this process, vapor-phase solutions are condensed to produce a solid-phase product. This method is employed when coatings are required to change the electrical, optical, mechanical, and thermal properties of various materials. Thermal energy is employed in this method to heat the gas existing in the chamber, resulting in the deposition process. Substance nanoparticle can be produced under well-defined conditions.

3.2.5: Sono-chemical Method

In this technique, nanostructured materials are synthesized using an ultrasonic bath. At room temperature, a solution comprising a suitable solvent and metal oxide precursor is thoroughly agitated for two hours. The solution thus obtained is then placed under ultrasonic bath irradiation for a specific time and temperature. In the

end, solution is centrifuged, filtered, and dried at a given temperature to get fine nanostructured materials.

3.3: Chemical reagents used in Synthesis

The chemical reagents employed in this research are as follows:

Chemicals	M(g/mol)	Elements	Atomic number	Valence states	Ionic radii (pm)
Cobalt nitrate hexahydrate Co(NO ₃) ₂ . 6H ₂ O	291.04	Co	27	+2, +3,+4	79/88.5, 68.5/75, 67
iron nitrate hexahydrate Fe(NO ₃) ₂ . 6H ₂ O	404	Fe	26	+2, +3,+4,+5	75/92, 69/78.5,72.5
ammonium metavanadate NH ₄ VO ₃	116.98	V	23	+2, +3,+4,+5	93, 78,72,68
Gadolinium(III) nitrate hexahydrate Gd(NO ₃) ₃ . 6H ₂ O	451.36	Gd	64	+3	107.8
Sodium hydroxide NaOH	40				

Table 3: Reagents, Formula, Molecular mass, and Radii of some common metal ions used in the synthesis of spinel ferrites

All the compounds were analytical grade and didn't need to be purified further. Coprecipitation method was used to prepare nanoparticles. The reagent aqueous solution is then combined with magnetic stirrer continuous shaking till a clear resulting solution is obtained. The precipitating agent NaOH was quickly added to metal solutions, causing precipitates to develop in the solution. For 30 minutes, the solution is held at room temperature with continuous stirring. The pH of the solution was kept in range 12.5 and 13.5. The solution was centrifuged at 8000rpm to remove as much water as possible, rinsed with water and ethanol to create precipitates free of sodium and chloride ions. The product was dried in an electric oven at 70°C for 24 hours. The sample was crushed homogenously in an agate and mortar until a fine powder was formed. The mortar and pestle were cleaned with ethanol before and after this procedure. The powder was then annealed in a muffle furnace for three hours at 500 °C and 900°C. This process is used to prepare eight samples.

3.4: Schematic diagram of samples preparation:

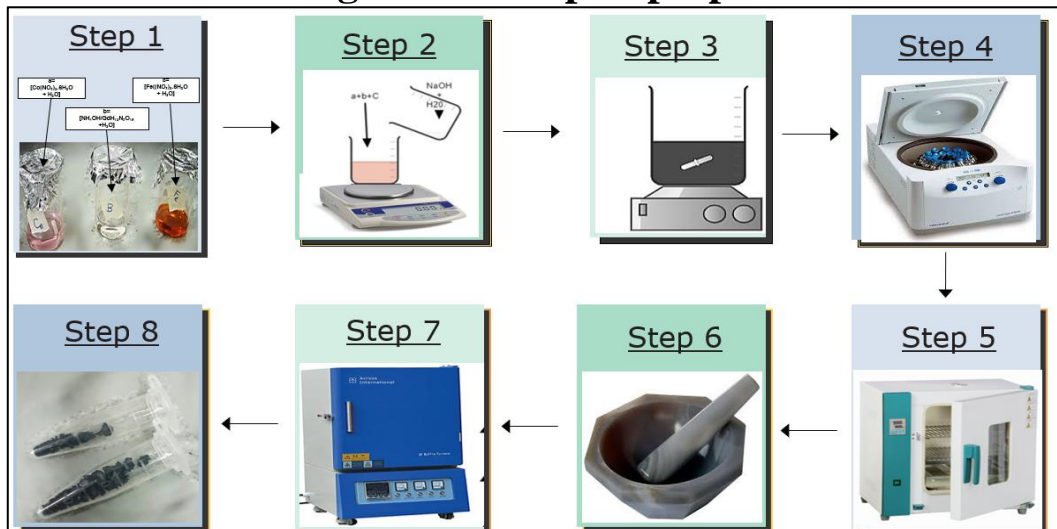


Figure 7: Schematic diagram of samples preparation

3.5: Characterization Techniques:

Specific methodologies are required to explore the various properties of ferrite nanoparticles. Furthermore, each technique yields distinct results, with some providing information on chemical and physical properties and others providing information on structure, morphology, and geometry. The techniques adopted for the characterization of the nanoparticle's samples are

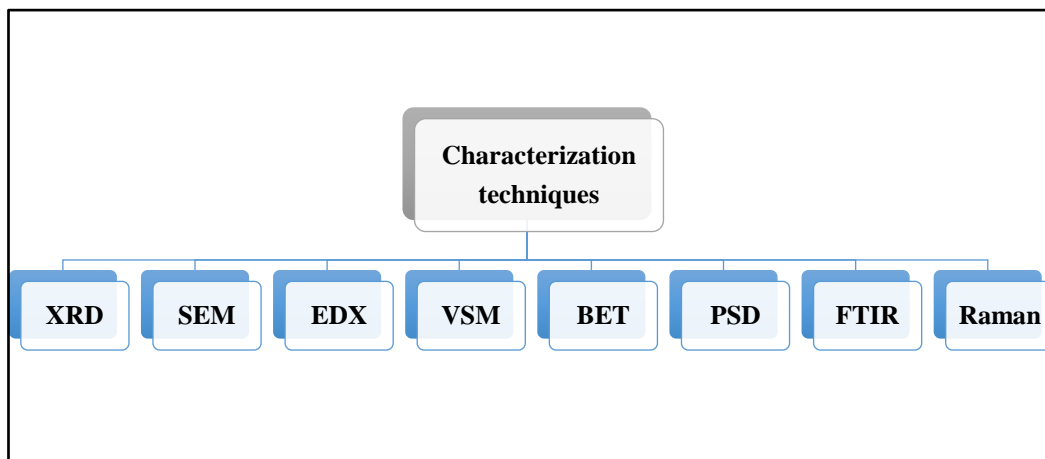


Figure 8: Characterisation Techniques

3.5.1: X-ray Diffraction

X-ray is a powerful, non-destructive method for evaluating the chemical structure and crystalline nature of natural and man-made materials. A crystal lattice is a three-dimensional pattern of atoms in space that is regular (cubic, rhombic, etc.). These are arranged into a series of parallel planes spaced by d (inter-planar or inter-atomic distance), which varies by substance. For each crystal, planes can be found in several orientations, each with its own d spacing.

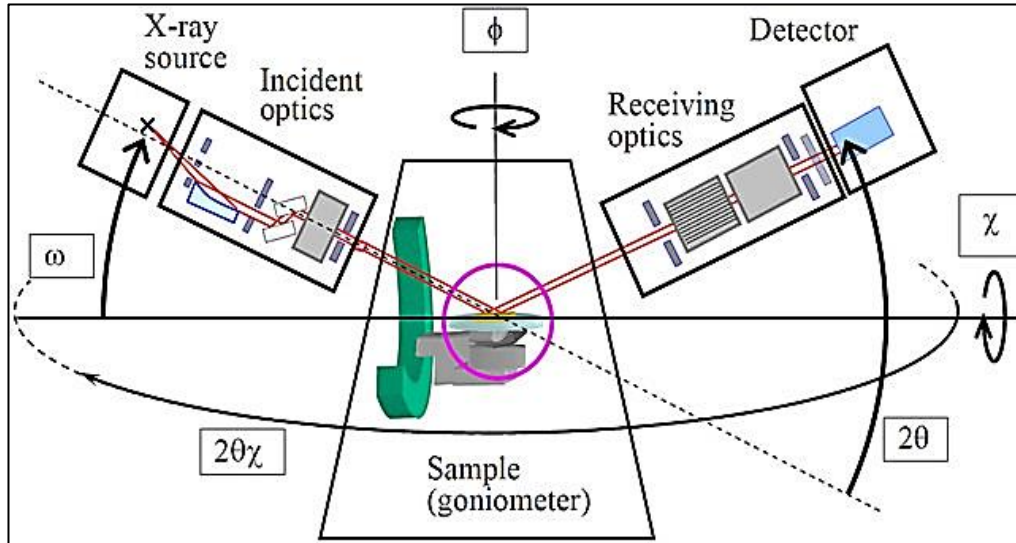


Figure 9: Description of X-ray Diffraction instruments

X-ray diffraction principles

The principle of constructive interference underpins XRD. Some photons from the incident beam are deflected away from the original direction of motion when X-ray photon collides with an electron. Diffracted waves from different atoms can interact and resulting intensity distribution is greatly altered as a result. Diffraction waves from different atoms can interact and resulting intensity distribution is greatly altered as a result. Diffraction from distinct atomic planes yields patterns that contain information about the atomic arrangement, position, intensity, width, and shapes of diffraction peaks in polycrystalline sample pattern. For each set of planes, there will be a small fraction of crystallites that are properly oriented to diffract. The peaks in the diffraction pattern are proportional to atomic distances.

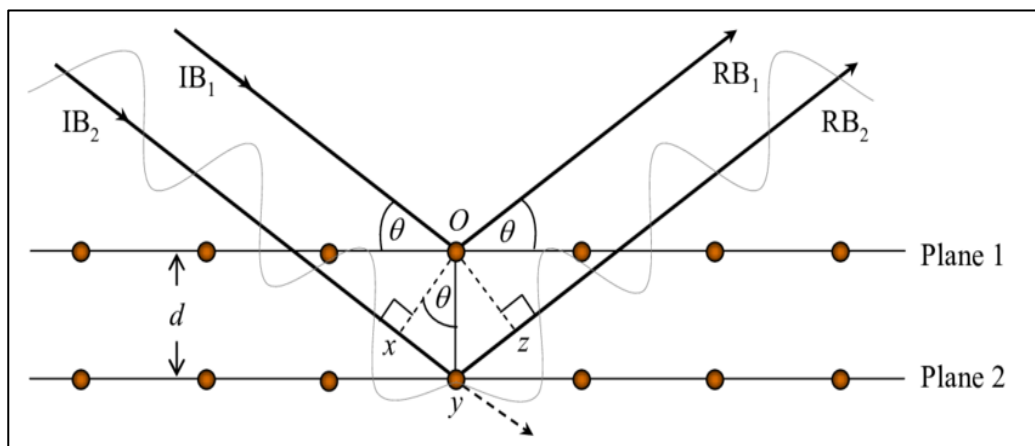


Figure 10: Principle of X-ray diffraction and illustrating Bragg's Law.

Structural analysis

Every crystalline material diffracts X-rays in a unique pattern and has a unique structure. By examining the peaks on the graph, we may determine if the material is crystalline or amorphous. If sharp intensity peaks are discovered, the material is crystalline, indicating a periodic character, whereas amorphous material only has one or two sharp peaks. The cell parameters are calculated by equation

$$d(hkl) = \frac{a}{\sqrt{h^2 + k^2 + l^2}}$$

The interplanar distance is denoted by d , and crystal indices denoted by miller indices(hkl). τ is the average crystallite size calculated from the broadening of peaks in XRD measurement using formula. λ denotes the wavelength of X-Ray radiation, β shows the FWHM of observed peaks.

$$\tau = \frac{0.9\lambda}{\beta \cos\theta}$$

$$\beta = \frac{1}{2}(2\theta_1 - 2\theta_2)$$

where β is full width at half maximum, τ is grain size and θ is diffraction angle.

$$\rho = (\sum A / N_A) / V$$

where ρ is unit cell density, V is volume, N_a is Avogadro's number, $\sum A$ is sum of atomic weights of all atoms.

The software "X'Pert High Score Plus" was used to calculate the lattice parameters. Calculated lattice parameters a , b and c are equal, with angles α , β and γ are equal to 90, indicating cubic crystal formation.

3.5.2 Scanning electron microscope

SEM was used to study surface morphology, and composition of the prepared samples. SEM images of samples are obtained by using electron beams of high energy scanned over the surface. Objective lenses and electromagnetic condenser were used to focus the electron beam of keV that interacts with the sample and produces a signal. These signals were collected, detected, and processed to form the image of the sample based on intensity having resolution lying in the range. The experimental set up for obtaining SEM images is displayed in Figure 3-5. To determine size and surface morphology, sample prepared by sonicating a small amount of sample in small volume of deionized water 10 ml for at least 30 minutes.

A drop of this mixture was poured on a glass substrate and dried. Later this substrate was placed on a carbon stub for gold sputtering using an Atomic Ion sputtering device, for making the sample conductive. The stub was then positioned in a vacuum chamber at low-pressure of Analytical Low Vacuum. Images taken at several various magnifications using an accelerating voltage of 20kV. To analyse distribution of colloids on substrate and surface morphology in thin films, various regions of the gradient films were marked by a simple marker and cut to separate each section. Each glass slide having a specific number of bilayers was placed on carbon stub and sputtered with a gold thin layer gradient to get high-resolution images of bilayer portions at different magnification.

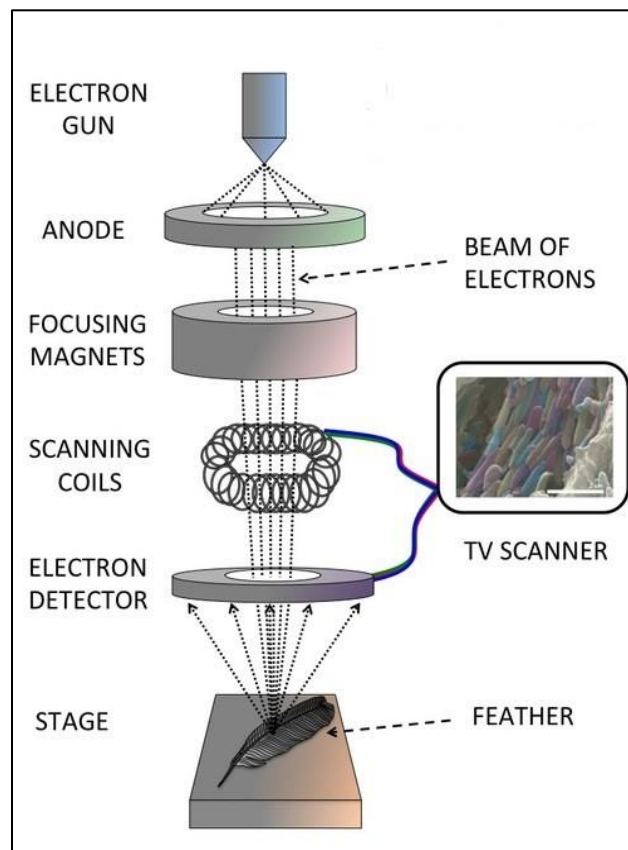


Figure 11: Schematic illustration of SEM instrument

3.5.3: Energy dispersive X-ray Spectroscopy (EDS)

The features of an EDS analyzer are:

Provides qualitative as well as quantitative analysis

Nondestructive technique requires little or no sample preparation

By striking the EDS detector, X-rays are produced in the form of charge pulses, which are then sorted based on voltage by attaching a charge sensitive pre-

amplifier. Finally, a spectrum of energy versus numbers is displayed on the screen.

3.5.4: Vibrating sample magnetometer

The VSM is used to study saturation magnetization and magnetic behaviour of the dried magnetic nanoparticles were studied. At RT magnetization measurement was carried out in constant field. Magnetic moments fluctuate with time by vibrating the sample that generates a signal by moving sample up and down that was sensed by coils, producing an output as hysteresis curve. It is the relationship between magnetic field intensity (B) and saturation magnetization (Ms) presented in Figure. Using software installed for monitoring, the system gives magnetization coercivity, and retentivity of the sample.

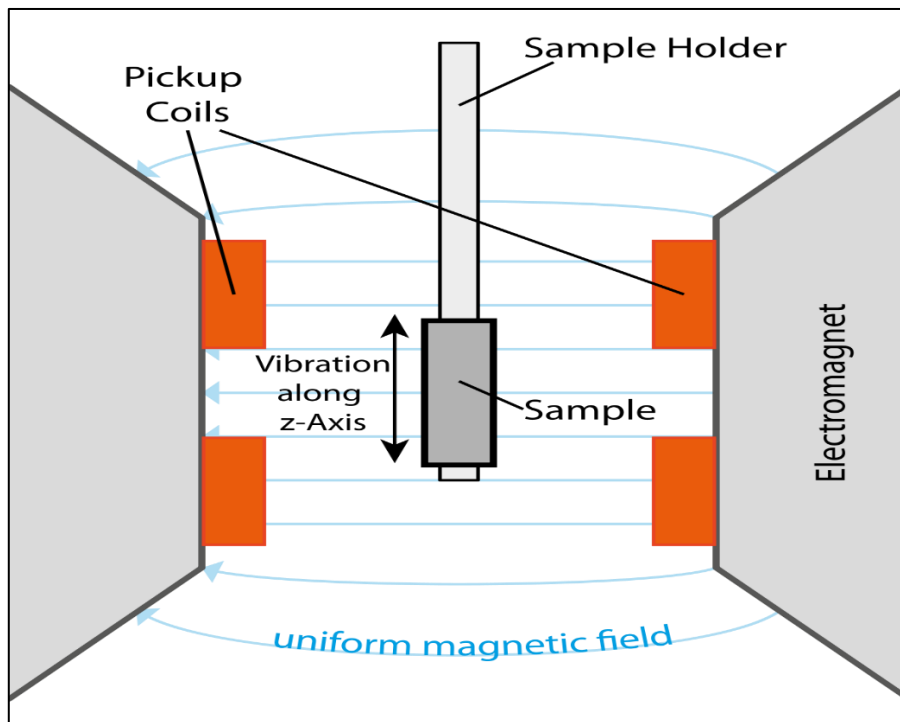


Figure 12: Vibrating sample magnetometer principle and working

The loop has a rectangular shape and exhibits irreversible changes of the magnetization.

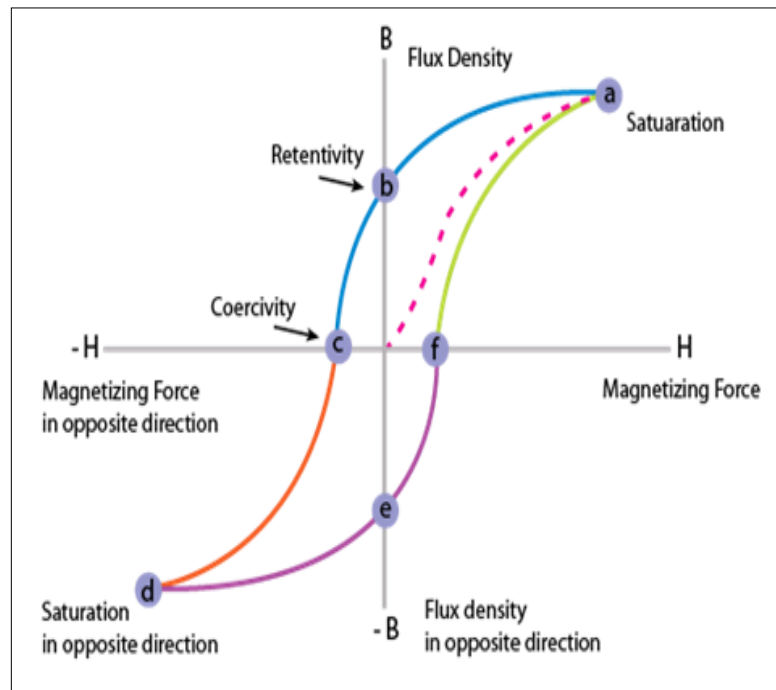


Figure 13 B-H hysteresis loop obtained from VSM

Saturation, remanence and coercivity

At high H, the intrinsic saturation is attained. The remanence is reached at zero-field. Coercivity is defined as the field necessary to reduce magnetization to zero after saturation

3.5.5: Brunauer-Emmet-Teller Theory (BET)

The physical adsorption of gas molecules on a solid surface is explained by BET. It is used to calculate the specific area of materials. Nitrogen is still the most utilised gaseous adsorbate for surface probing using BET techniques. As a result, routine BET analysis is often performed at the boiling temperature of N₂(77K). other adsorbates that are used include argon, carbon dioxide and water.

In Adsorption isothermal analysis the amount of gas adsorbed on the particle size is determined over a wide range of relative pressures at a constant temperature. The diameter of a pore is defined as its size. BET proposed a modal for determining the surface area of a nonporous solid that estimates the pore volume from the amount adsorbed at $p/p_0=0.99$ based on multilayer adsorption. BJH is a method for calculating the pore size distribution of a mesoporous solid based on the Kelvin

equation. The BJH algorithm is used to generate a pore size distribution graph. A single point volume in BET V is the total volume that is less than the greatest P/P₀. In BJH, V is a defined volume that indicates a volume at different pore diameters. Adsorption is confined to a monolayer of surface coverage, according to Langmuir theory. Because adsorption can only be one layer thick, the molecules must be distributed across a wide area. According to BET theory, the molecules can be adsorbed in multilayers. Molecules can be piled on top of each other to create a smaller space.

To determine specific area, BET theory is used to multilayer adsorption systems and typically employs probing gases that do not chemically react with material surface as adsorbates.

$$\text{specific surface area} = \frac{\text{total surface area of the material}}{\text{total volume or total mass}}$$

$$\text{Units} = \frac{m^2}{kg} \quad \text{or} \quad \frac{m^2}{m^3}$$

$$\text{Total surface area} = \frac{VmNs}{V}$$

N is Avogadro's number, s is effective cross-section area of one adsorbate molecule, V is molar volume and a is mass of adsorbent.

The BET Equation

$$\frac{1}{v\left(\frac{P_0}{P} - 1\right)} = \frac{1}{cv_m} + \frac{c-1}{cv_m} \frac{P}{P_0}$$

c is BET constant(dimensionless), $\frac{P_0}{P}$ is relative pressure, P is the equilibrium pressure and P₀ is the saturation or vapor pressure, V is the volume of gas adsorbed in milliliters, V_m is volume of gas adsorbed at STP to produce an apparent monolayer on the sample surface, in milliliters.

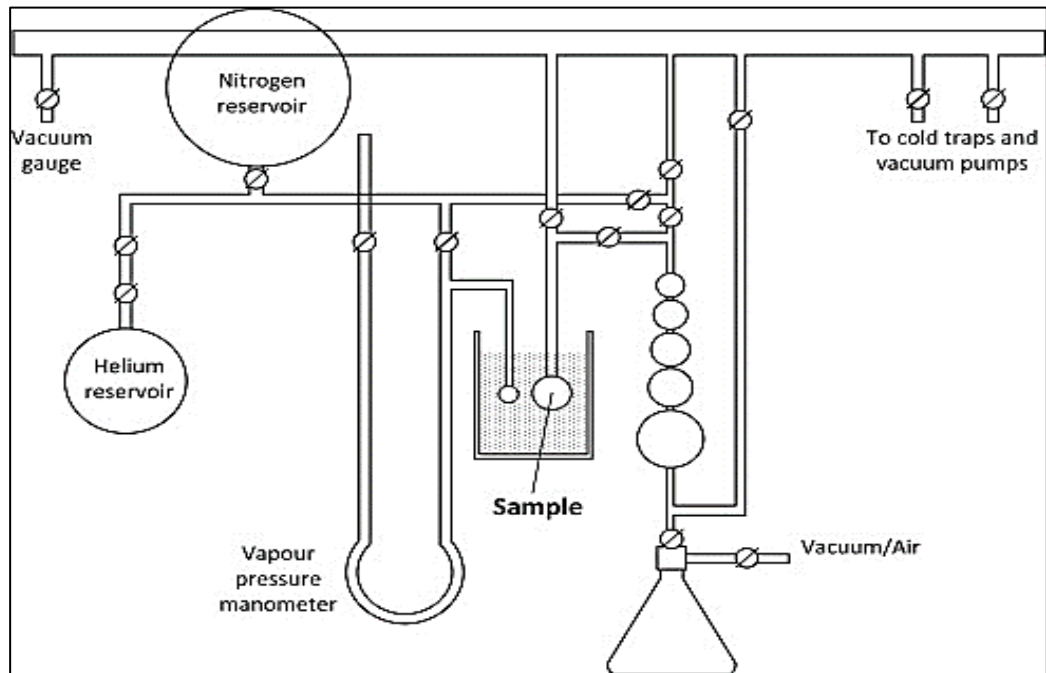


Figure 14: Schematic representation of BET surface area measurement instrument

3.5.6: Particle size distribution (PSD)

Particle size and size distribution are measured using PSD characterisation. This is an easy approach for analysing suspension stability and particle size is measured. Dry powder nanoparticles were weighted, dissolved in deionized water, and then sonicated for 30-40 minutes to assist in mixing and generating a homogenous dispersion. This method employs the use of a laser that is passed through the sample. Solution dispersion technology software is used for particle sizing.

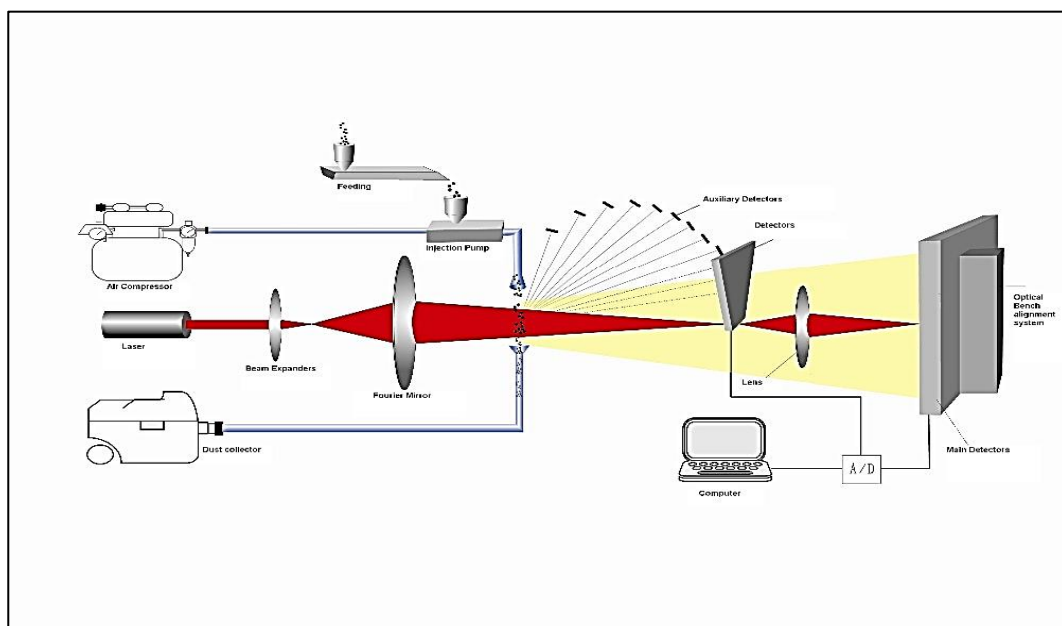


Figure 15: Laser Diffraction Particle size analysis principle

3.5.7: Fourier transform infrared spectroscopy (FTIR)

Atoms and molecules in solid materials vibrate to and fro about the mean point, and the vibrations depend on the bond length, atom mass, and bond angle with new atoms. Therefore, various solids have distinct vibrations. The energy of these vibrations is calculated below.

$$E_n = (n + \frac{1}{2}) \hbar \omega_0$$

$$E_0 = \frac{1}{2} \hbar \omega_0 \quad (n=0)$$

The above equation reflects the ground state energy, which is non-zero. Because vibrations of atoms or molecules are difficult to observe, we employ the FTIR technique to determine the vibrational modes. FTIR can also identify unknown materials and determine the number of components in a material, as well as the uniformity of a sample. The Michelson interferometer is essential in this approach because it separates IR radiations based on their wavelengths.

Because the frequency of IR radiation is comparable to the frequency of lattice vibration, we favour IR radiations in FTIR. When the frequency of the vibrational modes matches the frequency of the IR area, resonance occurs, and absorption peaks appear in the FTIR spectrum. However, when the frequency does not correspond to the IR area, infrared radiations pass through the sample without causing resonance.

Major components of FTIR are:

Interferometer

Infrared source

Infrared detector

Sample

Interferometer

Michelson interferometers are optical devices that are utilised in the FTIR technique. It is made up of three major components: a beam splitter, a moving

mirror (Mirror 2), and a fixed mirror (Mirror 1). Mirrors 1 and 2 are perpendicular to one another. Beam splitter, also known as semi-reflecting device, is in the centre of the interferometer.

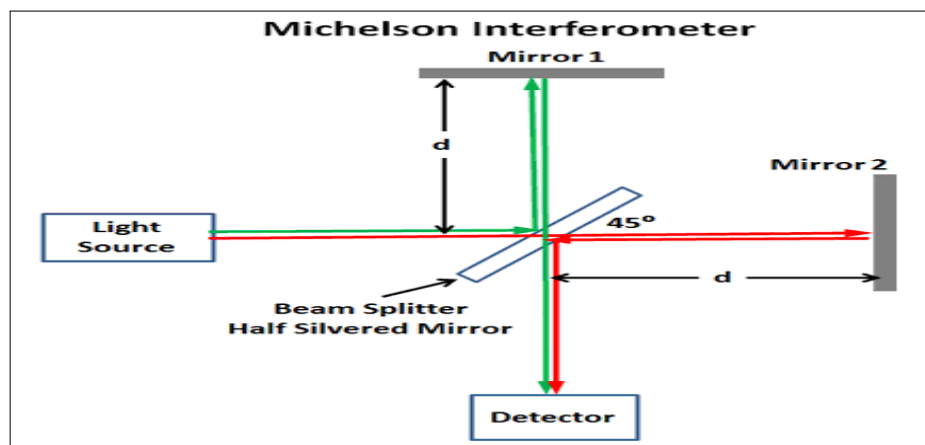


Figure 16: Block diagram of Michelson Interferometer Apparatus

Radiations are emitted by the light source, and the beam splitter divides them into half beams, which are then sent to moving and fixed mirrors. At the beam splitter, these two beams are reflected and recombined. Finally, an interference pattern is formed when these beams travel through the sample and are focused on the detector. The intensity varies sinusoidally and we get signals in time domain (interferogram) which are then converted to intensity versus frequency by Fourier transformation.

Experimental method of FTIR

The experimental procedure to study the vibrational modes of sample is as follows:

In the first step KBr pallets are used as background reference pallets. Then we add small number of particles of our superconducting sample in KBr which is mixed for 5-10 minutes. These pallets are then placed in a sample holder for absorption spectrum.

Using KBr spectrum as background we subtract it and get the spectrum of our superconducting material. Finally, the software OMNIC is used to analyse the vibrational modes of our material.

3.5.8: Raman spectroscopy

Non-destructive chemical analysis technique.

Used to obtain information about the molecules in a sample, e.g., chemical structure, phase, vibrational modes, etc.

Uses high power laser (monochromatic light).

Analysis of Raman spectra of material.

Suitable for solids, liquids, and gases.

No sample preparation required!

Depends upon the phenomenon of “Raman scattering” or “Raman effect”.

Majority of the high intensity laser light incident on an object is scattered without any change in its wavelength → **Rayleigh** or **elastic scattering**.

A small fraction (about 0.0001%) of light experiences change in wavelength → **Raman scattering**.

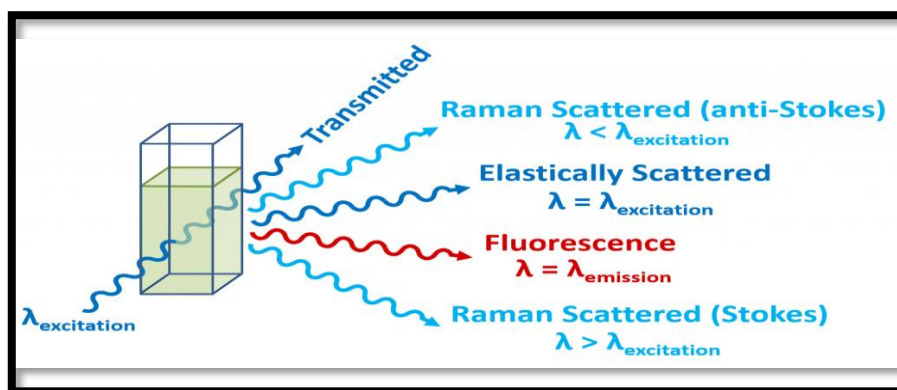
Change in wavelength and frequency → change in color of emitted light.

This energy shift is caused by interactions between the light photons and molecular vibrations (phonons) in the sample.

This fraction of “Raman scattered” light is the fingerprint that helps us determine the chemical and structural composition of the sample.

Emitted photon has lower frequency (and energy) → **Stokes shift**.

Emitted photon has higher frequency (and energy) → **Anti-Stokes shift**.



Raman effect

Raman effect is too weak to be observed visually. Highly sensitive spectrometer is used to analyze the light. Spectrometer filters and wavelength selectors block out the predominant Rayleigh Scattering to obtain a high-quality Raman spectrum.

Main components are:

Excitation source (laser)

Lenses to focus and collect the scattered light.

Filters to filter the effects of Rayleigh Scattering

High Quality Diffraction Grating

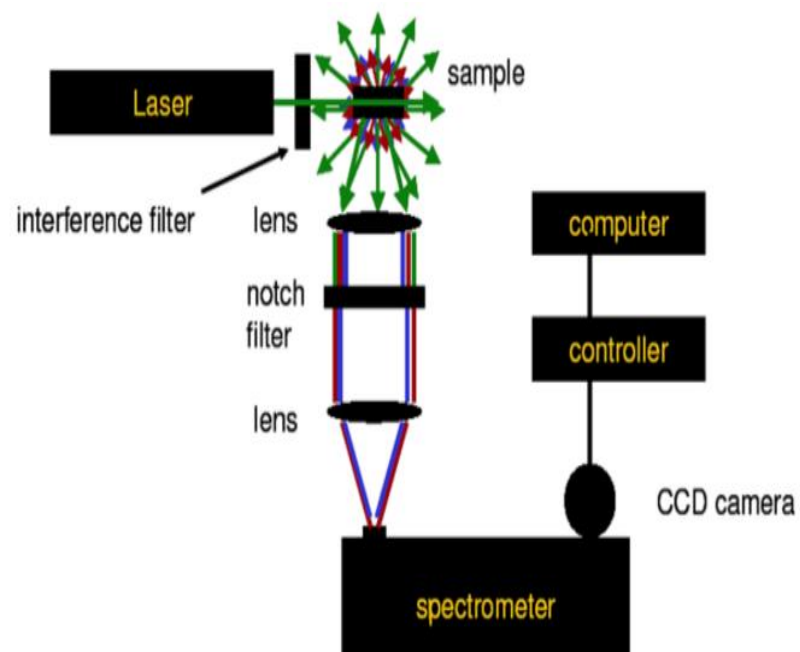


Figure 17: Schematic diagram of Raman Apparatus

Chapter 4: Results and Discussion

All the samples were characterized using various techniques.

4.1: Structural Analysis

XRD pattern was recorded at RT using a diffractometer with Cu-K α radiation having wavelength 1.5406 Å. Peaks observed at different diffraction angles were indexed as (200), (220), (311), (222), (400), (422), (511), (440) and (513). The peaks confirmed the creation of face-centered cubic crystal structure. The absence of secondary peak in ferrites implies the formation of a single cubic spinel structure. Due to improved crystallisation, the diffraction intensity rose with calcination temperature.

The lattice parameter “a” for CoV $_x$ Fe $_{2-x}$ O $_4$ declines nonlinearly indicating that the cation distribution has a significant impact on the lattice parameter. Vanadium ions, which predominantly reside at the octahedral sites as V $^{3+}$ (0.78 Å) replacing Fe $^{3+}$ (0.65 Å) at B-site, enhance the unit cell in Vanadium-containing samples. This mechanism, on the other hand, moves Fe $^{3+}$ from octahedral (0.65 Å) to tetrahedral (0.49 Å), decreasing unit cell. Because of the larger radii difference, the latter influence takes precedence, resulting in decrease in lattice parameter ‘a’. In CoV $_x$ Fe $_{2-x}$ O $_4$, the V $^{3+}$ ion replaces one iron ion, whereas each V $^{5+}$ ion replaces 1.67 Fe $^{3+}$ ions. This effectively generates many empty gaps, reducing crystalline size. [26]

Figure shows the lattice parameter with 2%, 5% and 10% Gd $^{3+}$ composition (x) in CoGd $_x$ Fe $_{2-x}$ O $_4$. As was shown, the values of ‘a’ increase as ‘x’ increased. It is the result of lattice swelling caused by the substitution of bigger Gd $^{3+}$ ions (0.938 Å) for smaller Fe $^{3+}$ ions (0.645 Å). Gd $^{3+}$ substituted Ni-Zn [28] and Mg-Mn [29] ferrites yielded similar results.

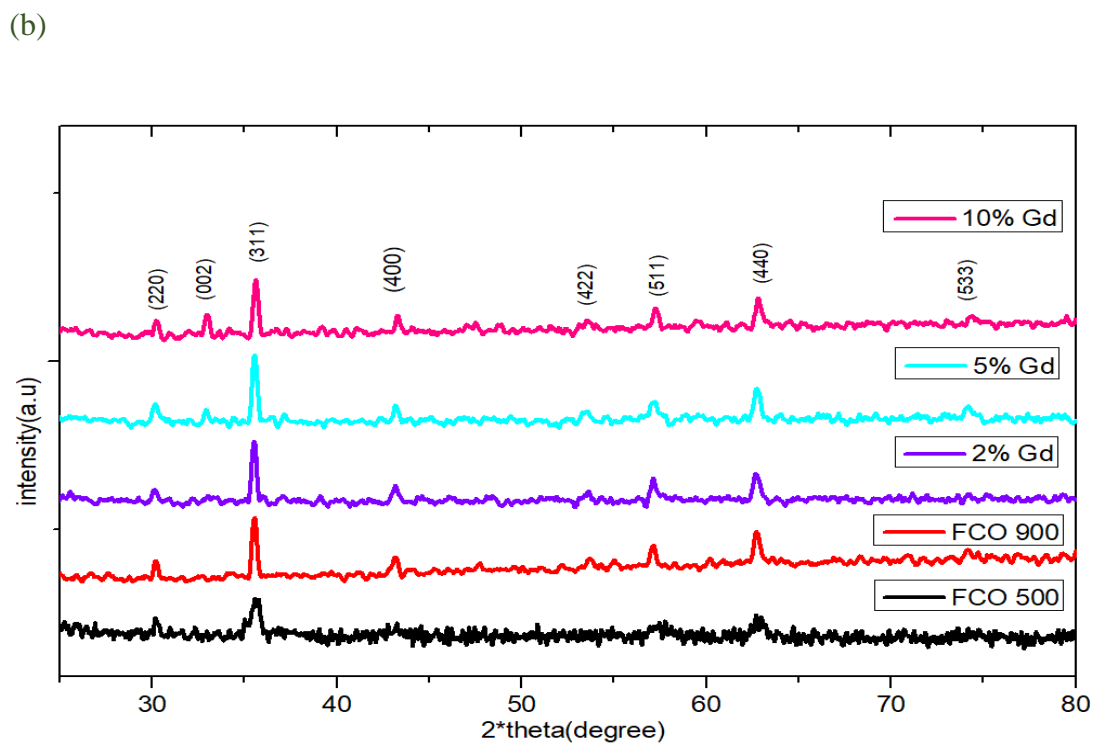
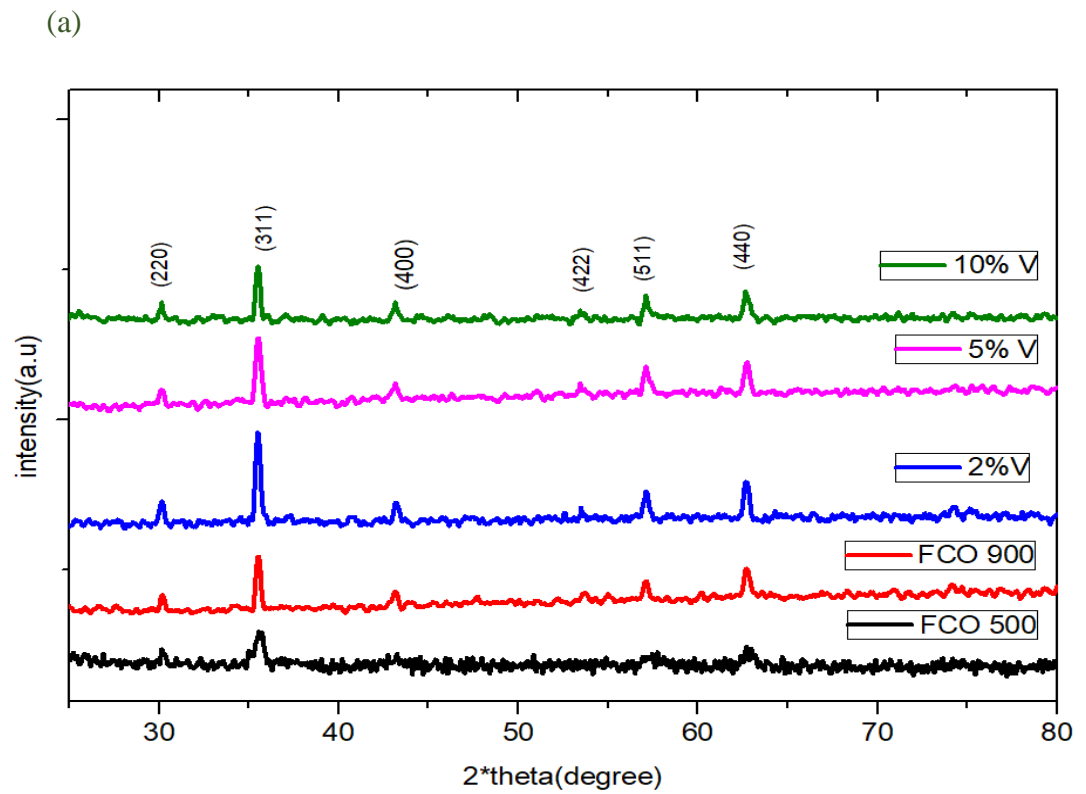
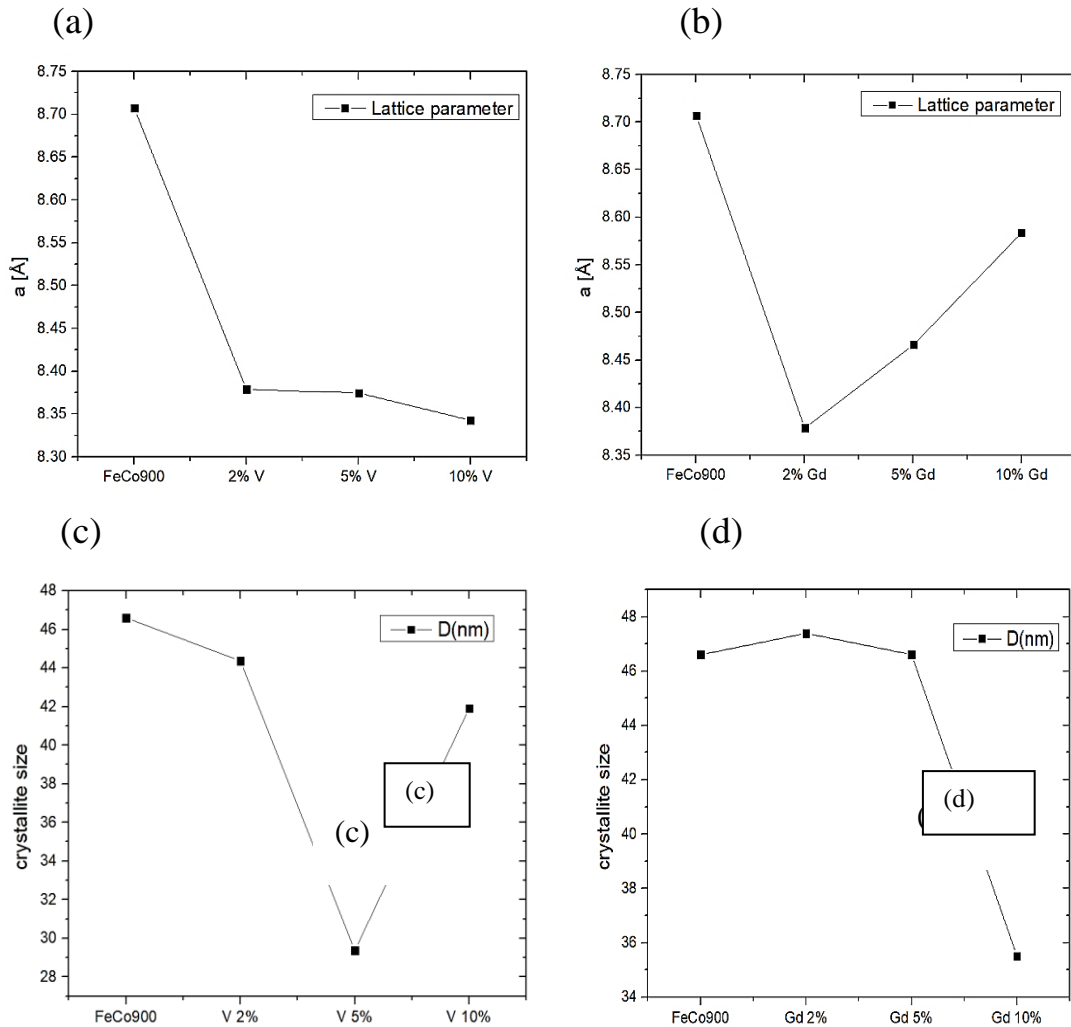


Figure 18: X-ray diffraction patterns obtained for (a) $\text{CoFe}_{2-x}\text{V}_x\text{O}_4$ (b) $\text{CoFe}_{2-x}\text{Gd}_x\text{O}_4$

Samples	$2*\theta$	β	d	$D(nm)$	$a[\text{\AA}]$	$V(a^3)$	$\rho(\text{gm/cm}^3)$
CFO500	35.59	0.45	2.52	18	8.350	583.08	5.34
CFO900	35.51	0.17	2.52	46	8.707	660.09	4.72
2% V	35.50	0.18	2.52	44	8.3787	588.20	5.29
5% V	35.59	0.28	2.52	39	8.3747	587.36	5.30
10% V	35.54	0.19	2.52	41	8.3427	580.65	5.35
2% Gd	35.49	0.17	2.52	47	8.3785	588.16	5.34
5% Gd	35.55	0.17	2.52	46	8.4658	606.74	5.24
10% Gd	35.56	0.23	2.52	35	8.5837	632.44	5.14

Table 4: XRD : peak positions, FWHM (β), interplanar distance (d), crystallite size (D), lattice parameter (a), Volume (V), Density (ρ) of prepared nanoparticles



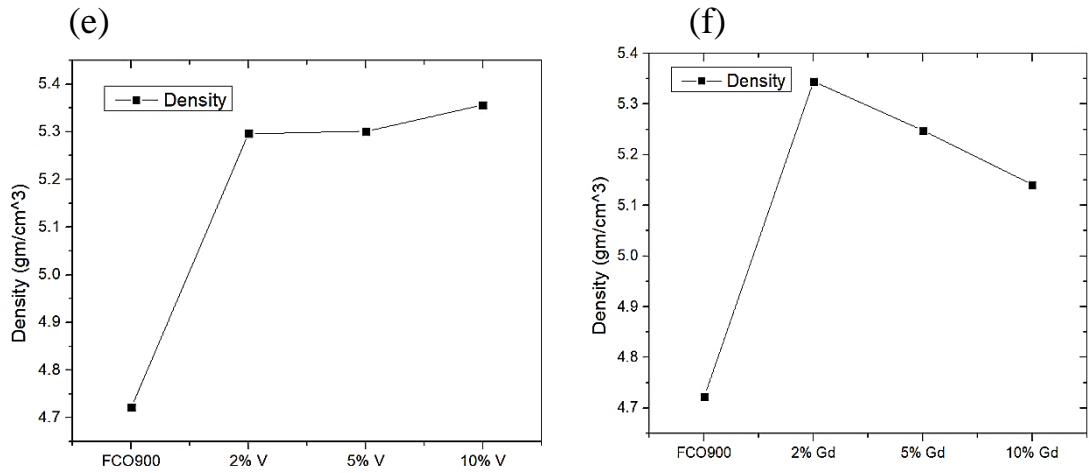


Figure 19: Variation of Crystallite size of (a) CVFO (b) CGFO, lattice parameter of (c) CVFO (d) CGFO, and X-ray density (e) CVFO (f) CGFO

4.2: Williamson Hall Analysis

Williamson Hall (WH) analysis was performed to obtain the crystallite size (D) and micro strain (ϵ) in both samples using the following equation:

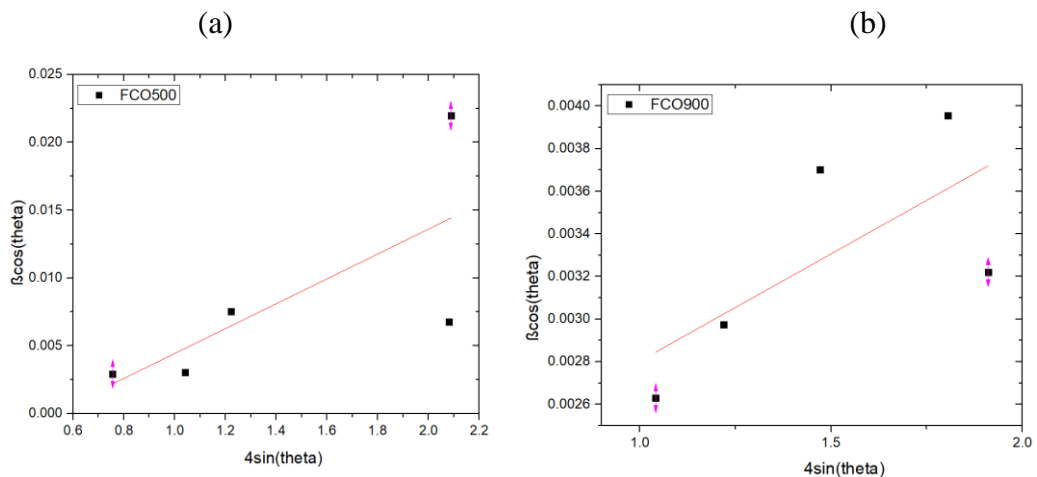
$$\beta_{tot} = \beta_{crystallite} + \beta_{strain}$$

$$\frac{\beta_{tot} \cos\theta}{k\lambda} = \epsilon \frac{4 \sin\theta}{k\lambda} + \frac{1}{D}$$

The slope and intercept of the graph between $\frac{\beta \cos\theta}{k\lambda}$ and $\frac{4 \sin\theta}{k\lambda}$ yields microstrain and crystallite size, respectively.

WH plot of CFO annealed at 500 degrees Celsius sample exhibits a clear contribution of strain effect.

Whereas the samples annealed at 900 degrees Celsius showed a non-linear plot which indicates the dominant crystallite size effect and less strain.



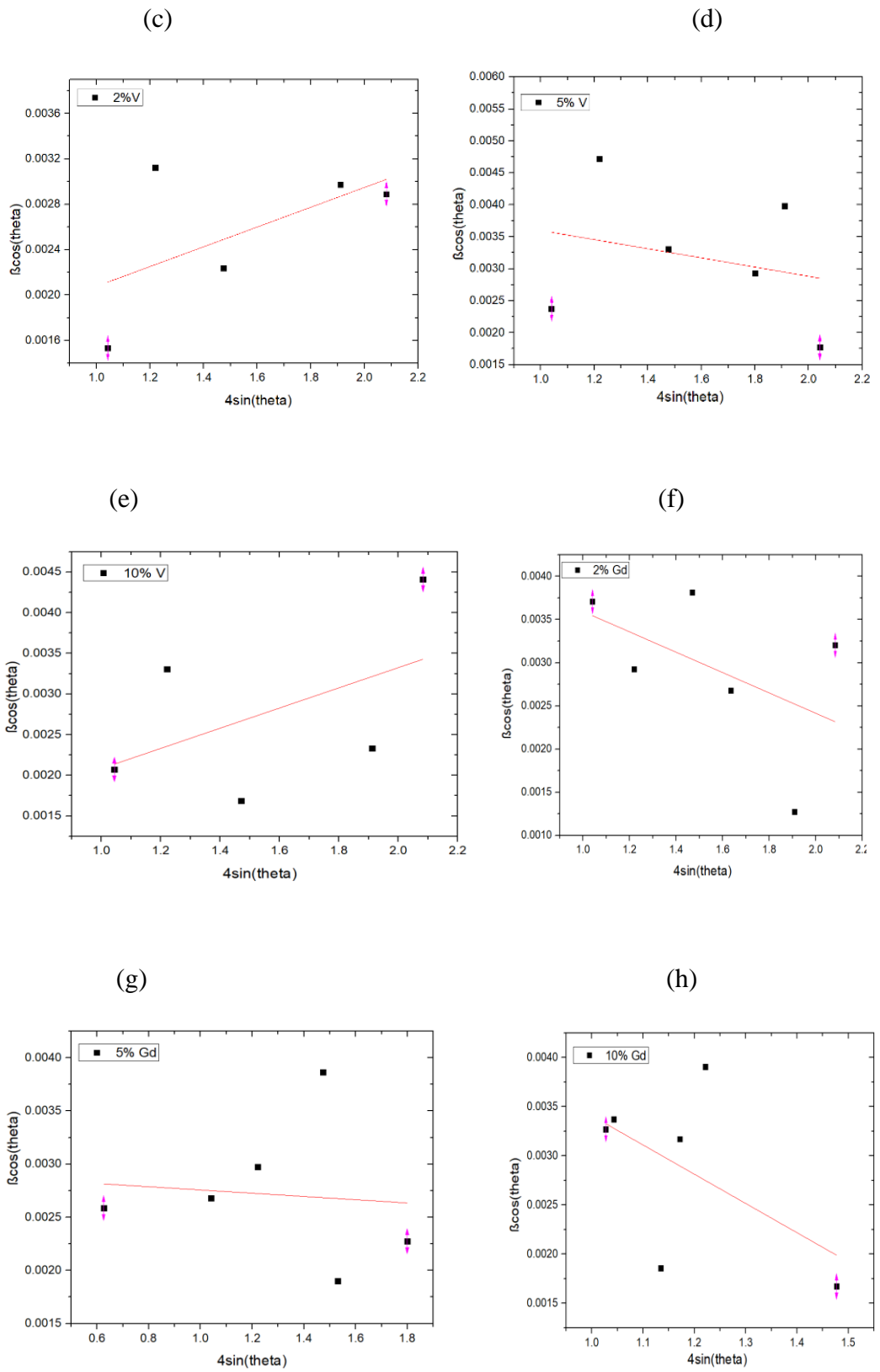


Figure 20: W-H plot of (a) CFO 500 (b) CFO 900 (c) V 2% (d) V 5% (e) V 10% (f) Gd 2% (g) Gd 5% (h) Gd 10%

4.3: Morphological and compositional Analysis

SEM results and EDX results of CoFe_2O_4

SEM and EDS patterns are used to analyse morphology and composition of the material formed. The SEM images shows that the composite of Cobalt and iron oxide formed by using co-precipitation method and sintered at 500 and 900 degrees Celsius is in nano range. EDX pattern clearly shows peaks of iron, Cobalt, and oxygen. EDX results shows compositional purity in figure.

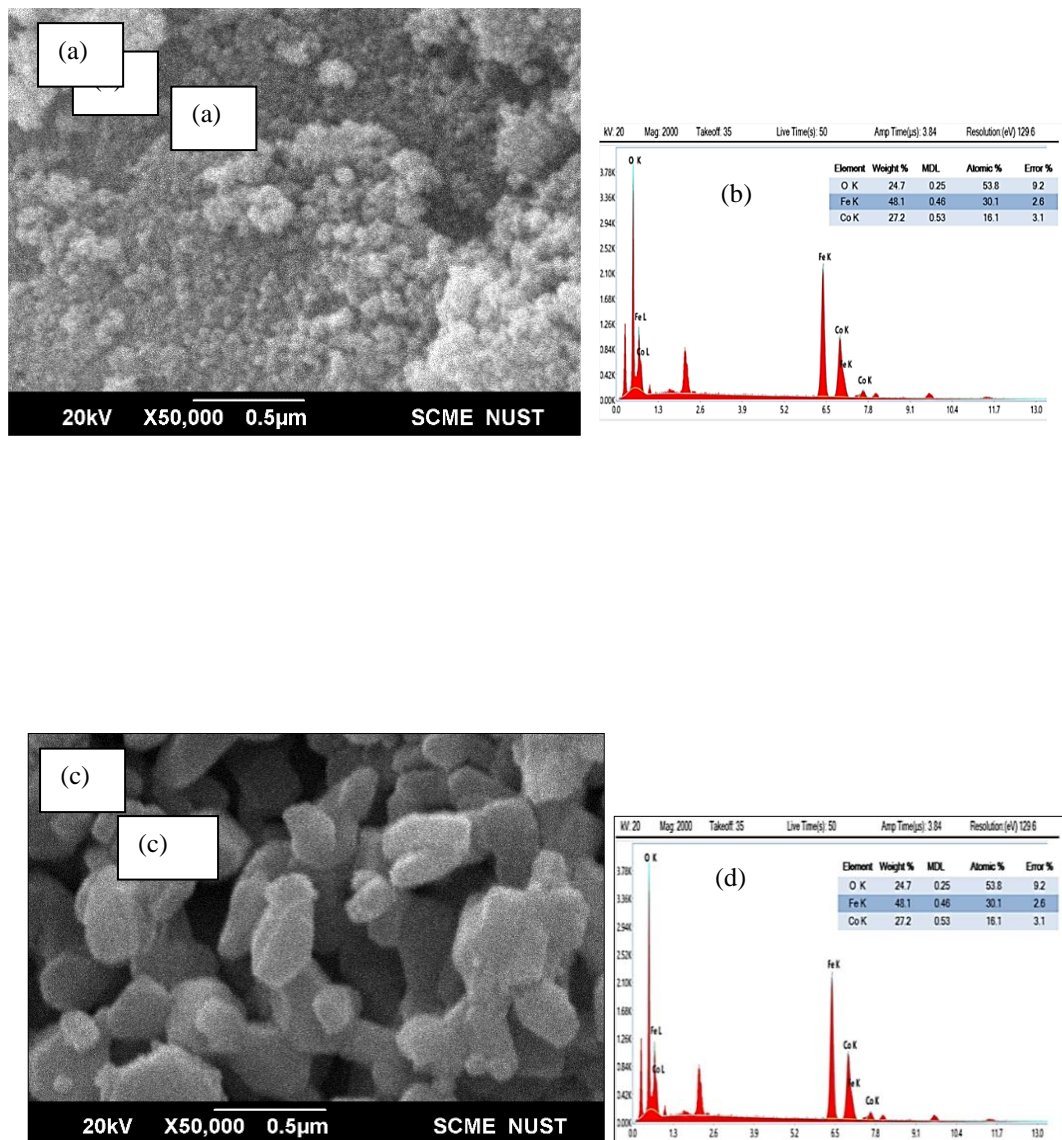
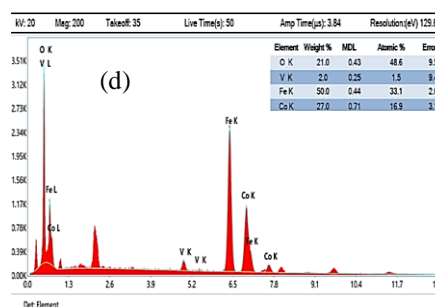
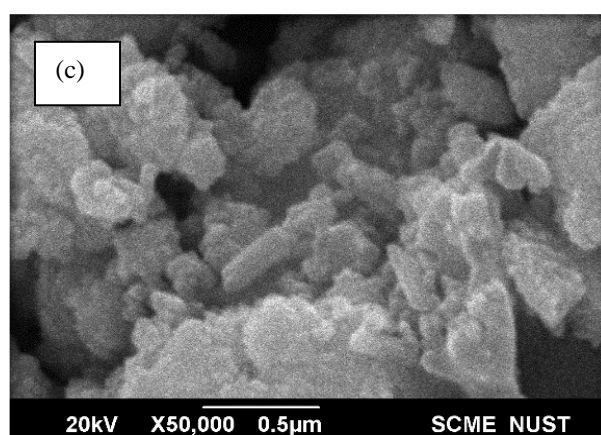
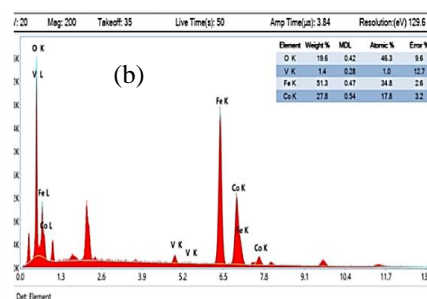
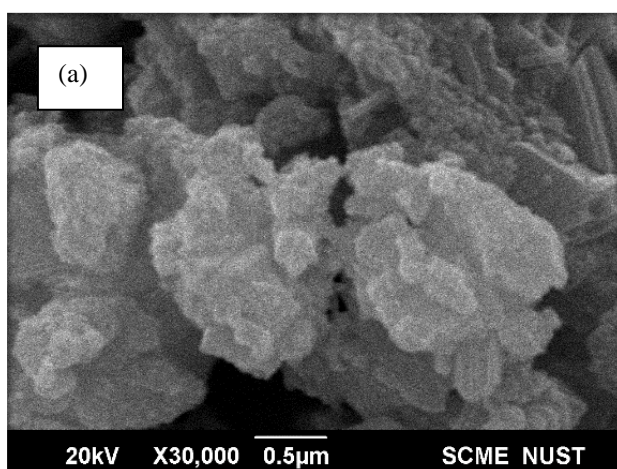


Figure 21: SEM micrographs and the corresponding EDX spectrum of (a,b) for CFO 500 (c,d) for CFO 900

Vanadium doped Cobalt ferrite

The SEM images and EDX spectrum of $\text{CoV}_x\text{Fe}_{2-x}\text{O}_4$ with 2%, 5% and 10% vanadium showed in figures. It is observed in figures that colonies of particles consist of small needle-like structure due to agglomeration. Due to inter linking connection network of particles is formed which helps the fast transportation of charge carriers i.e., photoinduced charges. This is expected due to the generation of electronic connections among the inter-linked particles during the growth of Fe_2O_3 thin films. The particles at the surface of thin films are uniformly distributed to form a compact surface. The interlinked particles have the porous structure which resulted in high internal surface area of the films. It is evident that the presence of such structure enabled the unique chemical and physical properties of the films and are potential features of the films showing higher photoelectrochemical water splitting efficiency.



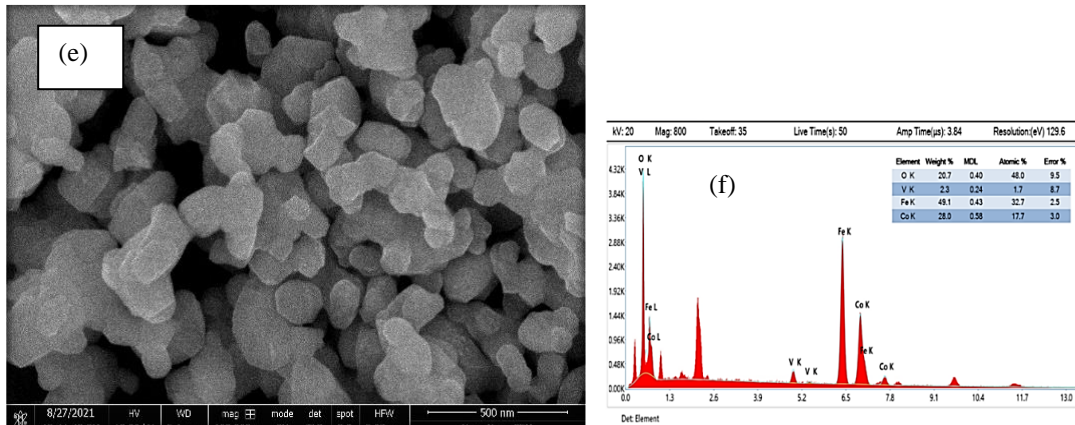
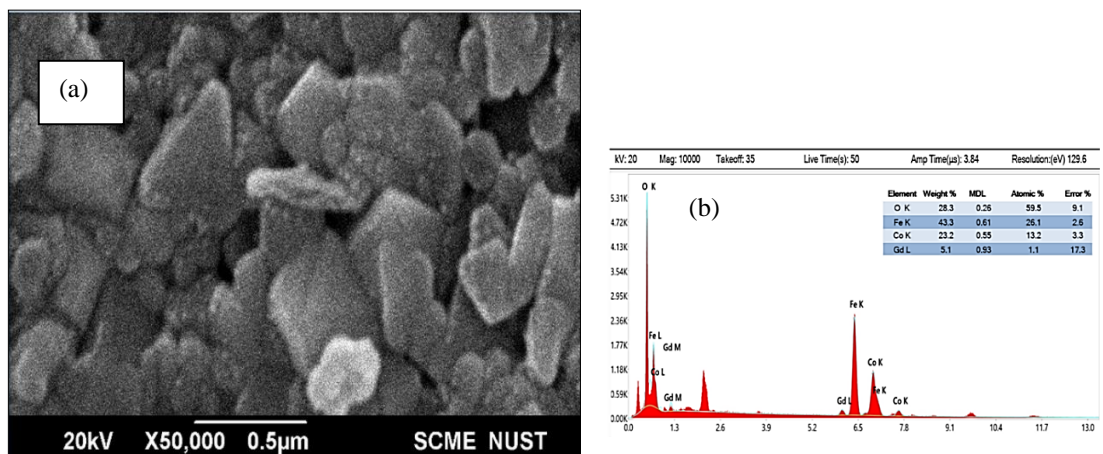


Figure 22: SEM micrographs and the corresponding EDS spectrum of (a,b) V 2% (c,d) V 5% (e,f) V 10%

Gadolinium doped Cobalt ferrite

The SEM images and EDX spectrum of $\text{CoV}_x\text{Gd}_{2-x}\text{O}_4$ with 2%, 5% and 10% Gadolinium showed in figures. The average crystallite size calculated using Scherrer formula is different as compared to the grain size which is expected because of the agglomeration of particles as can be seen from SEM images. SEM showed particles formed are in nano range. EDX spectrum showed purity of Gadolinium cobalt ferrite.



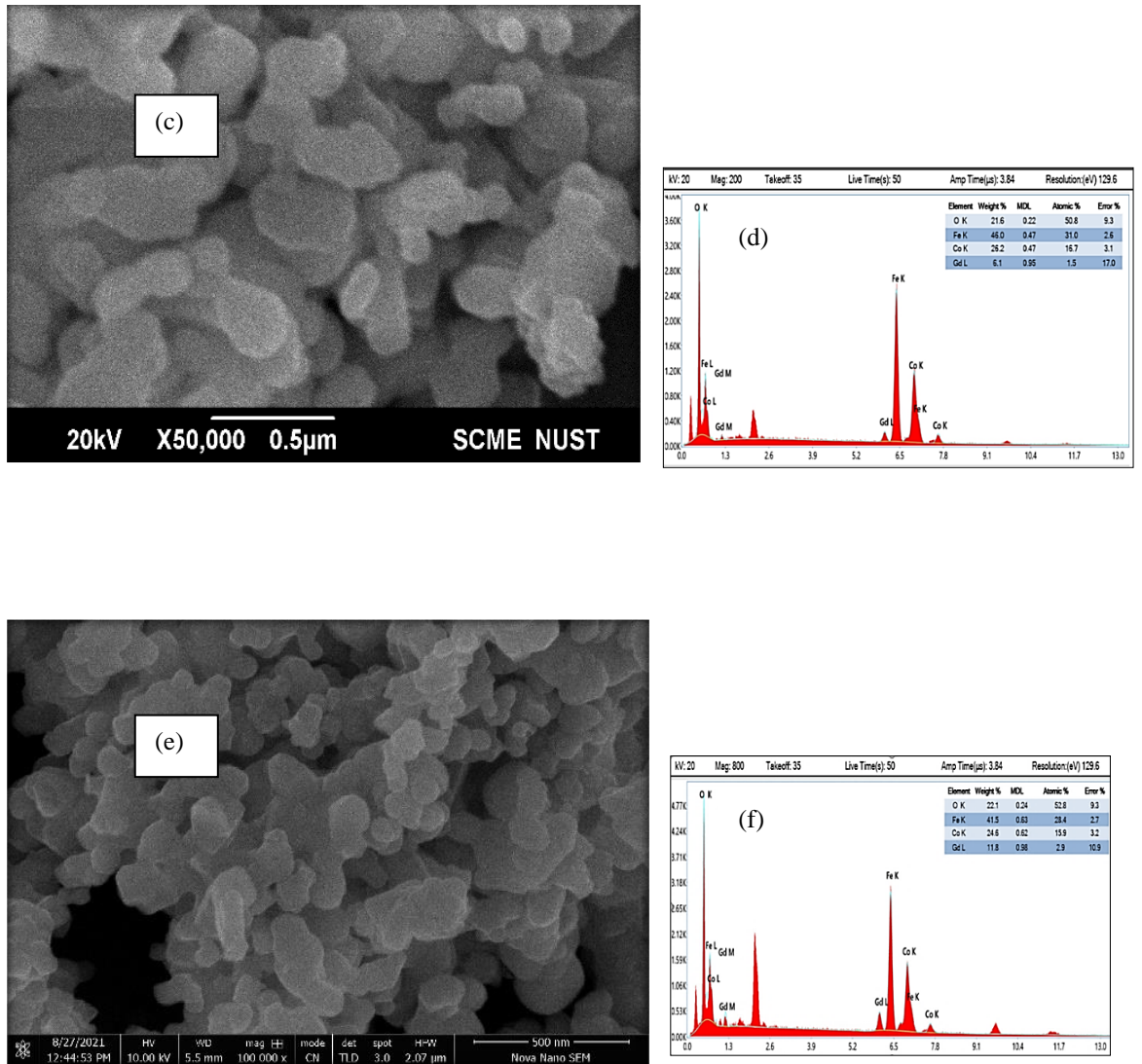


Figure 23: SEM micrographs and the corresponding EDS spectrum of (a,b) Gd 2% (c,d) Gd 5% (e,f) Gd 10%

4.4: Magnetic measurements

Vibrating sample magnetometer (VSM) is used to investigate magnetic characteristics. The magnetization (M-H) curves for undoped and doped cobalt ferrite is shown in Figure. The M-H hysteresis loops in cobalt ferrite clearly change with doping. Table shows the saturation magnetization (M_s), Coercivity (H_c), remnant magnetization (M_r) and remanence (M_r/M_s) ratio. The remanence ratio is a magnetic material properties parameter that describes how the magnetization orientation reorients to the nearby easy axis after the magnetic field removed. Magnetization does not pass through the origin in ferromagnetic materials; instead,

a magnetic field (M-H) loop forms. VSM results shows samples showed ferromagnetic behaviour. The change in values shows that Vanadium /Gadolinium doping of cobalt ferrite effected magnetic properties. [32]

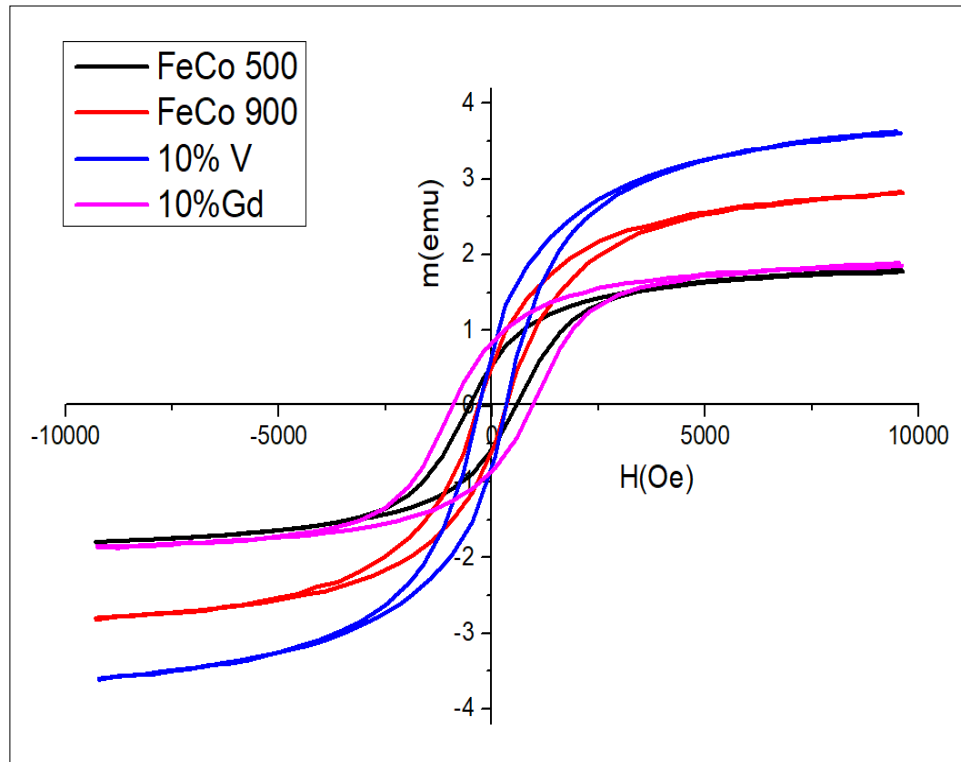


Figure 22: Room-temperature M-H loops for prepared nano samples

Samples	Hc (Oe)	Ms (emu)	Mr (emu)	K	μ	Mr/Ms
FCO900	328.4	2.816	0.553	963.32	0.1183	0.1964
10% V	313.14	3.607	0.728	1176.5	0.1615	0.2018
10% Gd	935.14	1.864	0.846	1815.7	0.087	0.4539

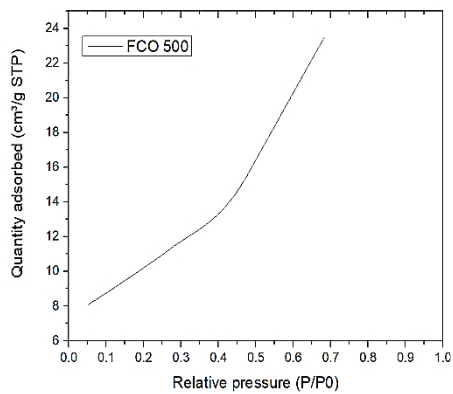
Table 5: Magnetic properties of samples, coercivity (H_c), saturation magnetization (M_s), remanent magnetization (M_r), magneto crystalline anisotropy (K), molecular mass (M), Magnetic moment(μ)

4.5: BET Analysis

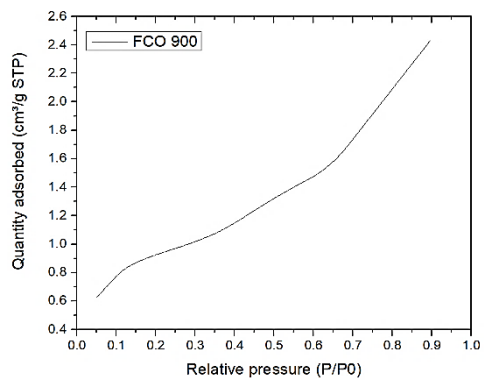
BET is used to calculate surface area and pore size distribution; adsorption isotherms were carried out using nitrogen gas.

Smaller grains result in more grain boundaries and higher porosity hence the decrease in particle size is also responsible for the increase in porosity. The porous nature of the ferrite is clearly seen in the SEM pictures.

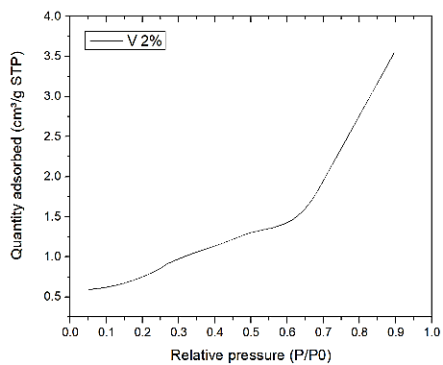
(a)



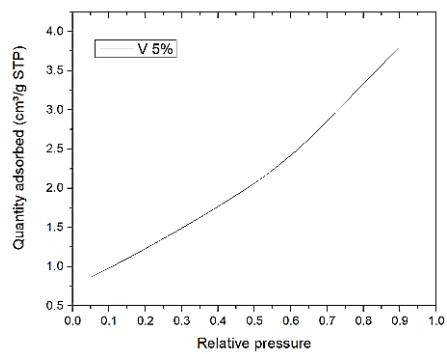
(b)



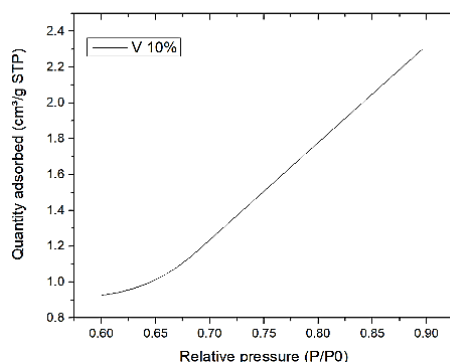
(c)



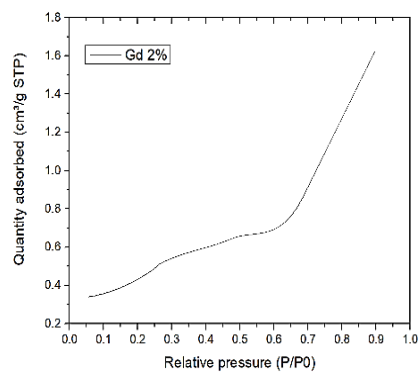
(d)



(e)



(f)



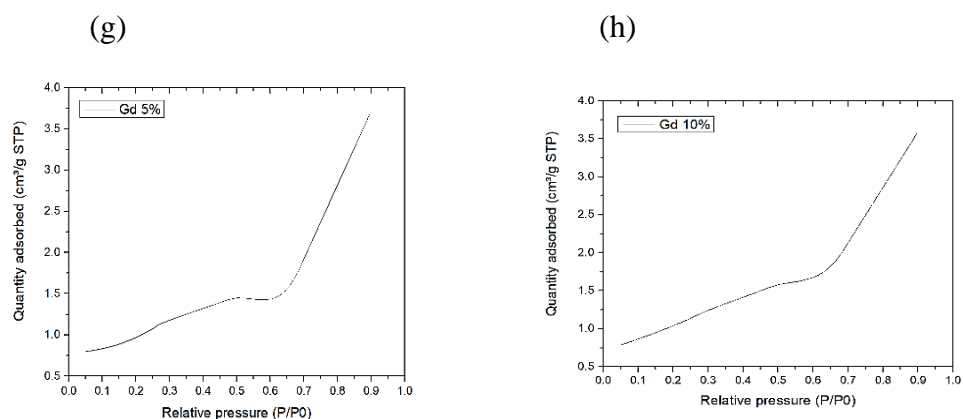


Figure 23:: BET adsorption isotherm of (a) CFO 500 (b) CFO 900 (c) V 2% (d) V 5% (e) V 10% (f) Gd 2% (g) Gd 5% (h) Gd 10%

4.6: Particle size distribution Measurements

Samples	Bet Surface Area (m ² /g)	Langmuir Surface Area(m ² /g)	BJH pore volume(cm ³ /g)	BJH pore size (Å)	Average particle size (Å) (BET)
FeCo900	1.34	13.64	0.003392	45.97	44541
2% V	2.93	4.32	0.0056	54.40	20464
5% V	4.65	7.04	0.005949	39.18	32881
10% V	1.18	13.70	0.00342	53.63	17539
2% Gd	1.66	2.45	0.002427	57.38	36059
5% Gd	3.59	5.24	0.005736	60.677	16676
10% Gd	1.89	20.08	0.005296	53.927	31712

Table 6: BET analysis of surface area, Langmuir surface area, BJH pore volume, BJH pore size, average particle size

PSD characterization is used to determine particle size and size distribution. This is a simple method for determining suspension stability and particle size in solution. Dry powder nanoparticles were weighed using an analytical mass scale, suspended in deionized water, and then sonicated for 30-40 minutes to assist in mixing and the formation of a homogeneous dispersion. This technique makes use of a laser that is passed through the sample. For particle sizing, solution dispersion technology software is employed. The mean diameter is calculated using software, which is given a measurement of the size ranges present in solution.

The PS results for particle size in solution are shown in the table. When all particles were disseminated in water, they tended to form agglomerates of varied sizes. Because the nanoparticles are uncoated, they agglomerate, with a diameter ranging from 2.5 to 9.5 micrometres.

Samples	Particle size(μm)
V2%	5.70
V5%	5.68
V10%	5.65
G2%	2.76
G5%	9.49
G10%	6.16

Table 7: Particle size distribution of V and Gd doped cobalt ferrite nanoparticles

4.6: FTIR spectroscopy

FTIR spectrum was obtained for CoFe_2O_4 , CoVFe_2O_4 , and $\text{CoGdFe}_2\text{O}_4$ nanocrystals in the 300cm^{-1} to 4000cm^{-1} range. The IR spectrum provide data on the chemical and molecular structure changes that occur in the produced ferrites during calcination treatments. The measured peaks are consistent with the literature results. In ferrite, the metallic ions are found in two types of sub-lattice positions: Tetrahedral (A) and Octahedral (B). Because of the stretching of these two lattice site configurations, the peak around two absorption bands ν_1 (500-460) and ν_2 (600-500) reflects Tetrahedral (A) and Octahedral (B) groups, respectively. [33] The presence of two sub-sublattice lines in the FTIR spectra, namely tetrahedral (A) and octahedral (B), confirmed the creation of a single-phase spinel structure. The observed ν_1 and ν_2 absorption bands are attributable to the metal-oxygen stretching vibration mode A and B sites. The discrepancies in positions of the 1 and 2 bonds can be traced to differences in the lengths of the Fe-O bonds at tetrahedral (A) and octahedral (B) sites.

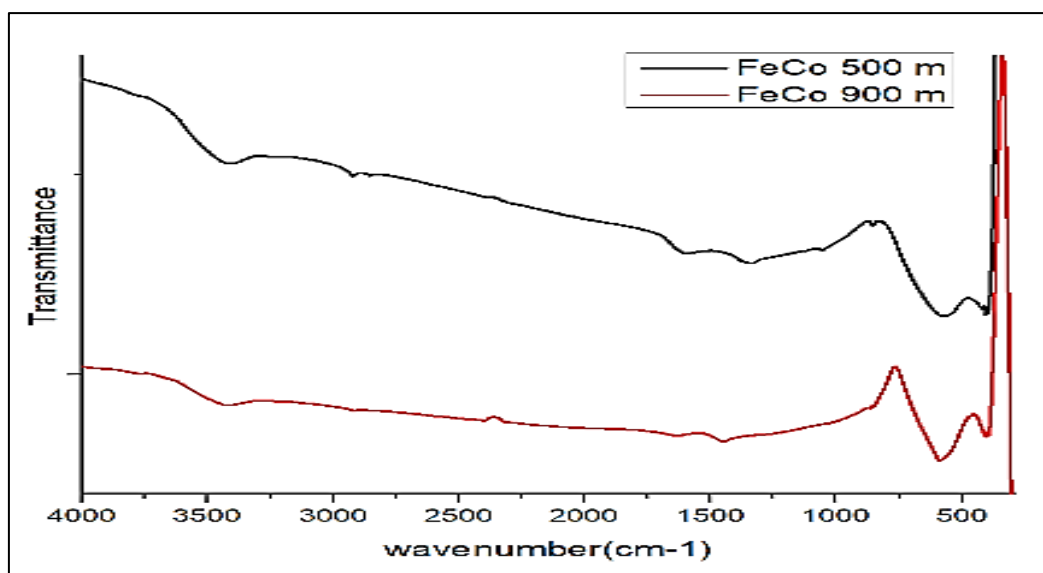
The wide band around 3400-3450 and infrared absorption around 1600 are caused by the fundamental and overtones OH stretching vibrations of hydroxyl groups of

water on the nanoparticles, respectively. [31] With increasing V/Gd-doping, both stretching vibrations modes of metal complex in tetrahedral and octahedral site slightly move toward higher frequencies side. This clearly shows that in the nanostructured V/Gd-doped cobalt ferrite, Co^{2+} is replaced by V/Gd ions.

FTIR results

Samples	FTIR peaks
CFO500	394,404,416,571,829,855,1058,1341,1589,2853,2922,3417
CFO900	393,405,587,850,1446,1634,2404,3417
V2%	394.13,404.27,409.07,577.11,1029.02,1626.89,2851,2921, 3410
V5%	381,391,401,585,1629,2316,2412,2850,2922,3429
V10%	378,394,402,585,1121,1437,1630,2920,3417
G2%	402.87,408,544,973
G5%	412,419,573
G10%	396,405,412,565,1015,3388

Table 8: Analysis of vibrational spectra FTIR of CFO500, CFO900, V and Gd doped CFO prepared samples



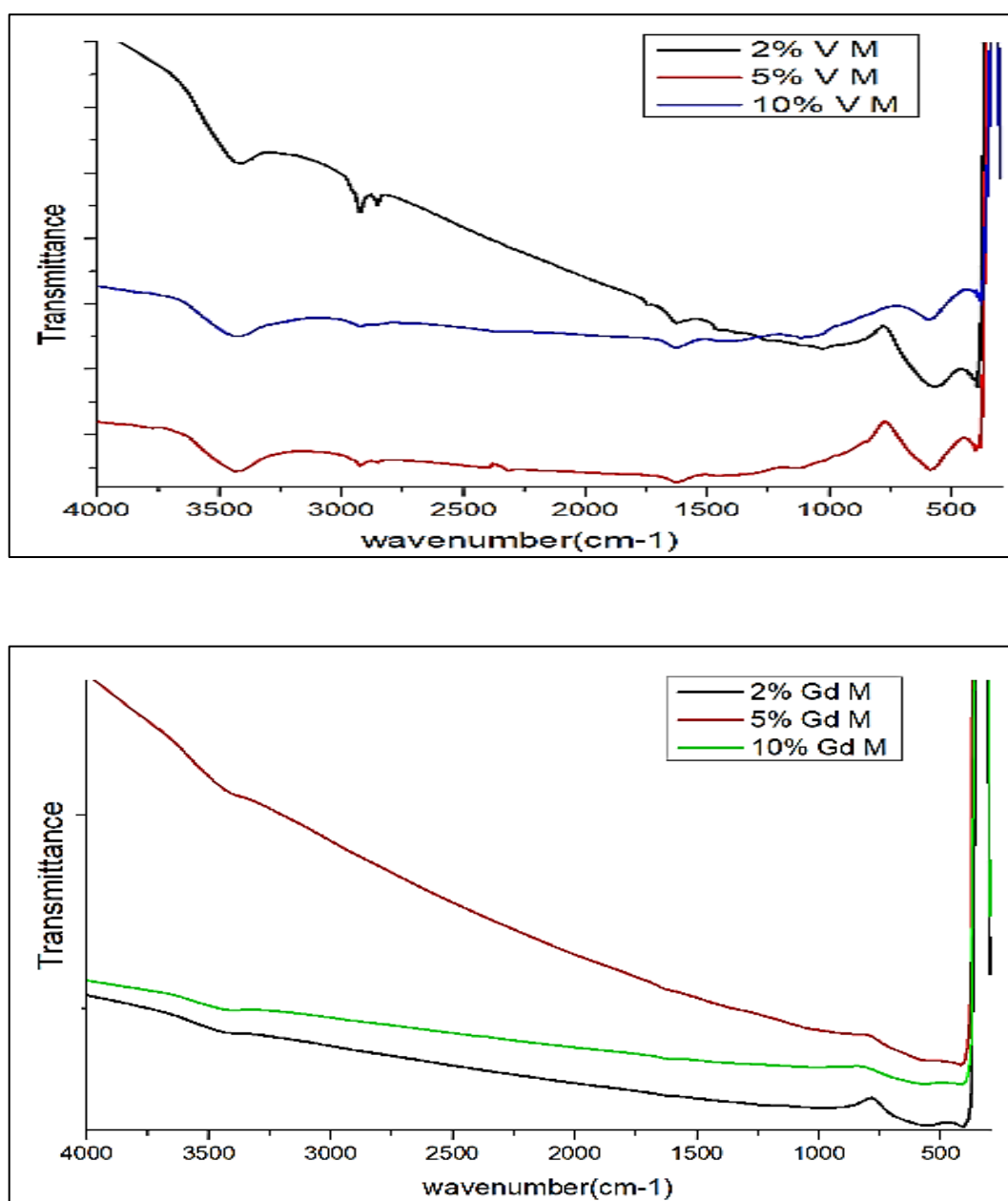


Figure 24: Infra-red absorption spectra of CFO500, CFO900, V and Gd doped CFO prepared samples

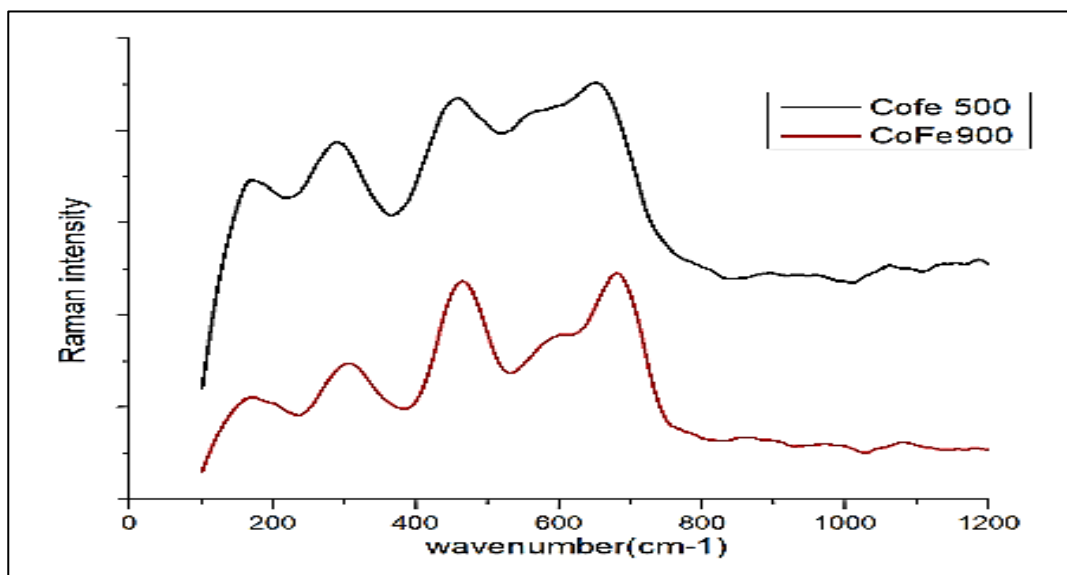
4.7: Raman Spectroscopy

Raman spectroscopy is a useful technique for studying the atomic structure of nanoparticles. [34] Figure depicts the Raman spectra of CoFe_2O_4 spinel ferrite nanoparticles. Group theory analysis predicts the following optical phonon distribution: $5T_{1u} + A_{1g} + E_g + 3T_{2g}$, with the $5T_{1u}$ modes being IR active and the other five modes ($A_{1g} + E_g + 3T_{2g}$) being Raman active and consisted of mobility of O ions and both A-site and B-site ions in the Spinel structure. [35] The A_{1g} mode is associated with symmetric oxygen anion stretching, the E_g mode with

symmetric oxygen anion bending, and the T_{2g} mode with tetrahedral and octahedral cations. [36]

The figure and table show that as made CoFe₂O₄ spinel ferrite nanoparticles exhibit Raman modes at ~198, ~297, ~461, ~558, ~604, and ~680 cm⁻¹ with a shoulder-like characteristic on the lower wavenumber side (604 cm⁻¹). By assigning these bands to A_{1g}(1) and A_{2g}(2) modes, the stretching vibrations of Fe-O and M-O bonds in tetrahedral sites were demonstrated. The T_{2g} and E_g Raman modes were given lower frequency modes (198, 297, 461, and 558 cm⁻¹) indicating spinel structural vibration. The figure and table demonstrate the Raman shift when Cobalt ferrite is doped. It is related to particle size change and cation redistribution in annealed CoFe₂O₄ spinel ferrite samples [34-36].

The change in intensity ratio with increasing annealing temperature is observed and recorded in a table.



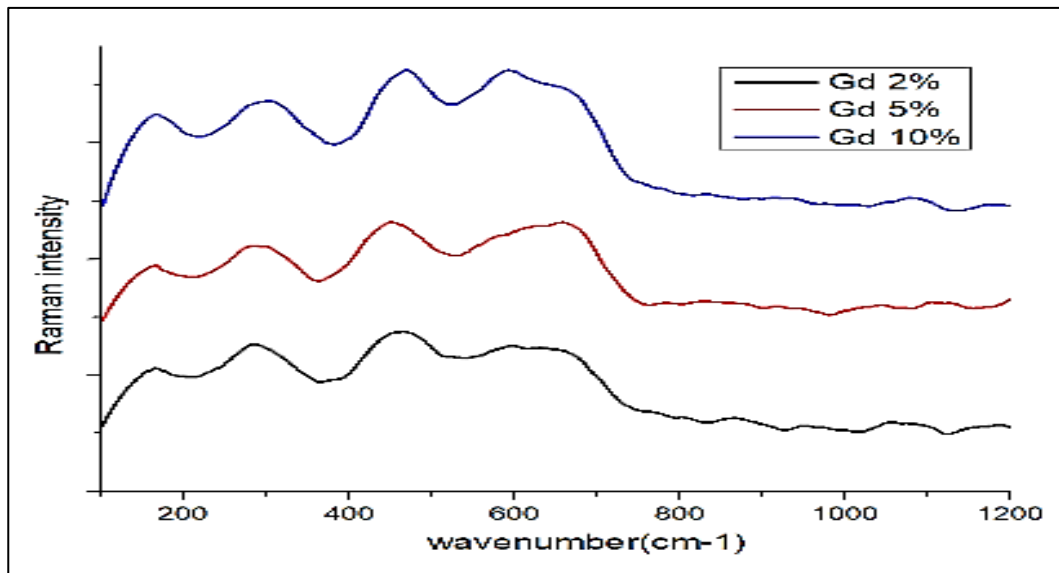
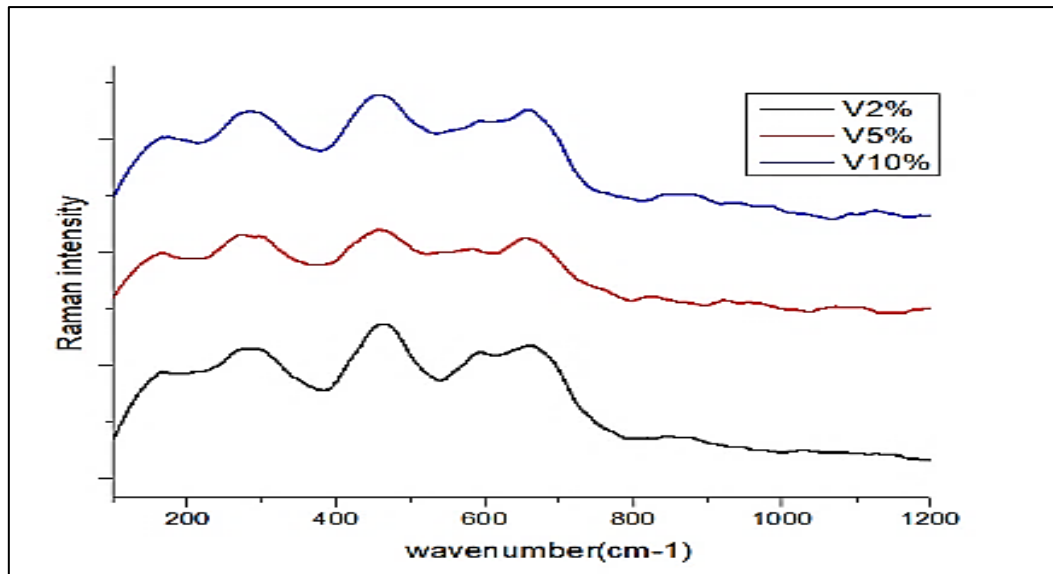


Figure 25: Raman spectra of CFO500, CFO900, V and Gd doped nano samples

Chapter 5: Conclusion

Co-precipitation was used to produce pure cobalt ferrite annealed at 500 and 900 degrees Celsius, as well as transition metal Vanadium (V^{3+}) and rare earth Gadolinium (Gd^{3+}) ions doped nanocrystalline cobalt ferrites chemically produced as $CoM_xFe_{2-x}O_4$, where M represents V or Gd and $x = 0\%$, 2% , 5% , and 10%). The powder X-ray diffraction technique was followed to characterise the ferrite samples. An X-ray diffractogram (XRD) analysis reveals the formation of a cubic spinel phase with no ambiguity peaks. The predicted particle size of the samples ranges from 18 nm to 48 nm. According to XRD measurements, the crystal structure improved with increasing annealing temperature. With V doping, particle size decreased and then increased. This is because V replaced iron in the octahedral location, reducing crystallite size; but as doping concentrations exceeded 5%, Fe began to move towards the tetrahedral site, increasing crystallite size. The size of crystallites was lowered via Gd replacement. SEM imaging was used to study the morphology of the ferrites. In SEM images, nanocrystalline particles can be seen arranged into layers with a porous structure. The presence of Co, Fe, V, and Gd elements in the samples was shown by EDX analysis. According to FTIR measurements, the vibrational peaks associated with octahedral and tetrahedral sites vary with doping. By PSD analysis, nanoparticle aggregation was discovered. The BET findings were used to calculate the specific surface area of samples, and the BET isotherm curve reflected layer-by-layer adsorption. Using VSM data, magnetic properties such as coercivity, retentivity, and saturation magnetization were determined. According to the VSM study, all the samples were ferromagnetic. Doping increased remanence magnetization. The lattice parameter "a" decreases with vanadium doping, as does cell volume, while density increases. When gadolinium is doped, the lattice parameter increases, as does cell volume and density. The coercivity value decreases with vanadium doping and increases with gadolinium doping. The magnitudes of several characteristics imply that the ferrites could be used in magnetic recording and storage systems.

References

- [1] Karak, N. (2018). *Nanomaterials and Polymer Nanocomposites: Raw Materials to Applications* (1st ed.). Elsevier.
- [2] *Nano-Glass Ceramics: Processing, Properties and Applications (Micro & Nano Technologies)* by Vahak Marghussian (2015-01-09). (1886). Elsevier Science Publishing Co Inc.
- [3] Spaldin, N. A., & Fiebig, M. (2005). The Renaissance of Magnetoelectric Multiferroics. *Science*, 309(5733), 391–392. <https://doi.org/10.1126/science.1113357>
- [4] Bedanta, S. and W. Kleemann, Supermagnetism. *Journal of Physics D: Applied Physics*, 42 (2008). 013001.
- [5] A. N. A. Y. M. S.H. MAHMOOD1*, *J. Solid State Phenomena* 232 (2014) 65-92.
- [6] Morin, F., Oxides which show a metal-to-insulator transition at the Neel temperature. *Physical Review Letters*, 3 (1959) 34.
- [7] Thompson, G. K., Evans, B. J. (1993). The structure–property relationships in M-type hexaferrites: Hyperfine interactions and bulk magnetic properties. *Journal of Applied Physics*, 73(10), 6295–6297. <https://doi.org/10.1063/1.352675>
- [8] Bilovol, V. and R. Martínez-García, Phase transformation of strontium hexagonal ferrite. *Journal of Physics and Chemistry of Solids*, **86** (2015) 131-137.
- [9] Mathew, D.S. and R.-S. Juang, *An overview of the structure and magnetism of spinel ferrite nanoparticles and their synthesis in microemulsions*. *Chemical Engineering Journal*, 2007. **129**(1-3): p. 51-65.

- [10] Hong, X., et al., A novel ternary hybrid electromagnetic wave-absorbing composite based on BaFe_{11.92}(LaNd)_{0.04}O₁₉-titanium dioxide/multiwalled carbon nanotubes/polythiophene. *Composites Science and Technology*, 117 (2015). 215-224.
- [11] Augustyn, V., P. Simon, and B. Dunn, Pseudocapacitive oxide materials for highrate electrochemical energy storage. *Energy & Environmental Science*, 7 (2014) 15971614.
- [12] F.S. Li, L. Wang, J.B. Wang, Q.G. Zhou, X.Z. Zhou, H.P. Kunkel, G. Williams, J. Magn. Mater. 268 (2004) 332.
- [13] El-Shobaky, G., Turkey, A., Mostafa, N., & Mohamed, S. (2010). Effect of preparation conditions on physicochemical, surface and catalytic properties of cobalt ferrite prepared by coprecipitation. *Journal of Alloys and Compounds*, 493(1–2), 415–422. <https://doi.org/10.1016/j.jallcom.2009.12.115>
- [14] Amiri, S., & Shokrollahi, H. (2013). The role of cobalt ferrite magnetic nanoparticles in medical science. *Materials Science and Engineering: C*, 33(1), 1–8. <https://doi.org/10.1016/j.msec.2012.09.003>
- [15] Gul, I., Amin, F., Abbasi, A., Anis-ur-Rehman, M., & Maqsood, A. (2007). Physical and magnetic characterization of co-precipitated nanosize Co–Ni ferrites. *Scripta Materialia*, 56(6), 497–500. <https://doi.org/10.1016/j.scriptamat.2006.11.020>
- [16] Gul, I., Abbasi, A., Amin, F., Anis-ur-Rehman, M., & Maqsood, A. (2007). Structural, magnetic and electrical properties of Co_{1-x}Zn_xFe₂O₄ synthesized by co-precipitation method. *Journal of Magnetism and Magnetic Materials*, 311(2), 494–499. <https://doi.org/10.1016/j.jmmm.2006.08.005>
- [17] Goyal, A., Bansal, S., Samuel, P., Kumar, V., & Singhal, S. (2014). CoMn_{0.2}Fe_{1.8}O₄ferrite nanoparticles engineered by sol–gel technology: an expert and

versatile catalyst for the reduction of nitroaromatic compounds. *J. Mater. Chem. A*, 2(44), 18848–18860. <https://doi.org/10.1039/c4ta03900a>

[18] Melo, R. S., Banerjee, P., & Franco, A. (2018). Hydrothermal synthesis of nickel doped cobalt ferrite nanoparticles: optical and magnetic properties. *Journal of Materials Science: Materials in Electronics*, 29(17), 14657–14667.

[19] Zagaynov, I., Fedorov, S., & Goldberg, M. (2019). Electrical properties of Cu-Mn-Zr co-doped ceria electrolytes for intermediate temperature solid oxide fuel cell application. *Processing and Application of Ceramics*, 13(3), 244–249. <https://doi.org/10.2298/pac1903244z>

[20] Nohair, M., Perriat, P., Domenichini, B., & Gillot, B. (1994). Cationic distribution and mechanism of the oxidation of V³⁺ ions in vanadium-substituted magnetites. *Thermochimica Acta*, 244, 223–234. [https://doi.org/10.1016/0040-6031\(94\)80221-1](https://doi.org/10.1016/0040-6031(94)80221-1)

[21] Heiba, Z. K., Mohamed, M. B., & Ahmed, S. (2017). Cation distribution correlated with magnetic properties of cobalt ferrite nanoparticles defective by vanadium doping. *Journal of Magnetism and Magnetic Materials*, 441, 409–416. <https://doi.org/10.1016/j.jmmm.2017.06.021>

[22] Imanipour, P., Hasani, S., Seifoddini, A., Farnia, A., Karimabadi, F., Jahanbani-Ardakani, K., & Davar, F. (2020). The possibility of vanadium substitution on Co lattice sites in CoFe₂O₄ synthesized by sol–gel autocombustion method. *Journal of Sol-Gel Science and Technology*, 95(1), 157–167. <https://doi.org/10.1007/s10971-020-05316-w>

[23] Hossain, A., Esha, I. N., Elius, I. B., Khan, M. N. I., & Maria, K. H. (2020). Interrelation between cationic distribution and electromagnetic properties of vanadium-substituted Mn–Zn ferrites. *Journal of Materials Science: Materials in Electronics*, 32(1), 977–992. <https://doi.org/10.1007/s10854-020-04874-7>

[24] Sodaee, T., Ghasemi, A., & Razavi, R. S. (2015). Microstructural Characteristics and Magnetic Properties of Gadolinium-Substituted Cobalt Ferrite

Nanocrystals Synthesized by Hydrothermal Processing. *Journal of Cluster Science*, 27(4), 1239–1251. <https://doi.org/10.1007/s10876-015-0925-3>

[25] Mugutkar, A. B., Gore, S. K., Mane, R. S., Batoo, K. M., Adil, S. F., & Jadhav, S. S. (2018). Magneto-structural behaviour of Gd doped nanocrystalline Co-Zn ferrites governed by domain wall movement and spin rotations. *Ceramics International*, 44(17), 21675–21683. <https://doi.org/10.1016/j.ceramint.2018.08.255>

[26] Heiba, Z. K., Mohamed, M. B., & Ahmed, S. (2017). Cation distribution correlated with magnetic properties of cobalt ferrite nanoparticles defective by vanadium doping. *Journal of Magnetism and Magnetic Materials*, 441, 409–416. <https://doi.org/10.1016/j.jmmm.2017.06.021>

[27] Mugutkar, A. B., Gore, S. K., Mane, R. S., Batoo, K. M., Adil, S. F., & Jadhav, S. S. (2018). Magneto-structural behaviour of Gd doped nanocrystalline Co-Zn ferrites governed by domain wall movement and spin rotations. *Ceramics International*, 44(17), 21675–21683. <https://doi.org/10.1016/j.ceramint.2018.08.255>

[28] Kumar, A., Shen, J., Yang, W., Zhao, H., Sharma, P., Varshney, D., & Li, Q. (2017). Impact of Rare Earth Gd³⁺ Ions on Structural and Magnetic Properties of Ni_{0.5}Zn_{0.5}Fe_{2-x}Gd_xO₄ Spinel Ferrite: Useful for Advanced Spintronic Technologies. *Journal of Superconductivity and Novel Magnetism*, 31(4), 1173–1182. <https://doi.org/10.1007/s10948-017-4273-4>

[29] Kumar, G., Shah, J., Kotnala, R., Singh, V. P., Sarveena, Garg, G., Shirsath, S. E., Batoo, K. M., & Singh, M. (2015). Superparamagnetic behaviour and evidence of weakening in super-exchange interactions with the substitution of Gd³⁺ ions in the Mg–Mn nanoferrite matrix. *Materials Research Bulletin*, 63, 216–225. <https://doi.org/10.1016/j.materresbull.2014.12.009>

[30] Waldron, R. D. (1955). Infrared Spectra of Ferrites. *Physical Review*, 99(6), 1727–1735. <https://doi.org/10.1103/physrev.99.1727>

- [31] Franco, Sacco, de Marco, & Vaiano. (2019). Zinc Oxide Nanoparticles Obtained by Supercritical Antisolvent Precipitation for the Photocatalytic Degradation of Crystal Violet Dye. *Catalysts*, 9(4), 346. <https://doi.org/10.3390/catal9040346>
- [32] Puli, V. S., Adireddy, S., & Ramana, C. (2015). Chemical bonding and magnetic properties of gadolinium (Gd) substituted cobalt ferrite. *Journal of Alloys and Compounds*, 644, 470–475. <https://doi.org/10.1016/j.jallcom.2015.05.031>
- [33] Imanipour, P., Hasani, S., Seifoddini, A., Farnia, A., Karimabadi, F., Jahanbani-Ardakani, K., & Davar, F. (2020). The possibility of vanadium substitution on Co lattice sites in CoFe₂O₄ synthesized by sol–gel autocombustion method. *Journal of Sol-Gel Science and Technology*, 95(1), 157–167. <https://doi.org/10.1007/s10971-020-05316-w>
- [34] Baraliya, J., & Joshi, H. (2014). Spectroscopy investigation of nanometric cobalt ferrite synthesized by different techniques. *Vibrational Spectroscopy*, 74, 75–80. <https://doi.org/10.1016/j.vibspec.2014.07.013>
- [35] Chandramohan, P., Srinivasan, M., Velmurugan, S., & Narasimhan, S. (2011). Cation distribution and particle size effect on Raman spectrum of CoFe₂O₄. *Journal of Solid-State Chemistry*, 184(1), 89–96. <https://doi.org/10.1016/j.jssc.2010.10.019>
- [36] Yu, T., Shen, Z. X., Shi, Y., & Ding, J. (2002). Cation migration and magnetic ordering in spinel CoFe₂O₄ powder: micro-Raman scattering study. *Journal of Physics: Condensed Matter*, 14(37), L613–L618. <https://doi.org/10.1088/0953-8984/14/37/101>